

Oil & Natural Gas Technology

DOE Award No.: DE-FE0013531

Quarterly Research Performance Progress Report (Period ending 06/30/2016)

**Assessing the response of methane hydrates to environmental
change at the Svalbard continental margin**
Project Period (11/1/2013 to 10/31/2016)

Submitted by:
Marta E. Torres



Oregon State University
DUNS #: 053599908
104 COAS Admin. Bldg.
Corvallis, OR 97331-5503
e-mail: mtorres@coas.oregonstate.edu
Phone number: (541) 737-2902

Prepared for:
United States Department of Energy
National Energy Technology Laboratory



Office of Fossil Energy

EXECUTIVE SUMMARY

In November 2013, Oregon State University initiated the project entitled: **Assessing the response of methane hydrates to environmental change at the Svalbard continental margin.** In this project, we will take advantage of a unique opportunity to collect samples from the Svalbard continental margin. The overall objective of this research is to constrain the biogeochemical response of the gas hydrate system on the Svalbard margin to environmental change. Because of a delay in the planned expedition, we reconfigured the program based on discussions with NETL program managers and submitted a revised SOPO. In the new plan, we will collect samples in three expeditions, the first of which happened Oct 7-21, 2014. We were able to also join an expedition to the area onboard the RV Helmer Hanssen during May 15-29, 2015 and two other expeditions one onboard the RV Heincke August-September 2015, and June 2016. We completed a modification of the SOPO to include participation in an upcoming MeBo drilling expedition in this region, scheduled for August-September, 2016. We continue with analyses of the samples collected during these expeditions as well as completed a computational model for methane hydrate formation under conditions of variable salinity, two papers on the modeling efforts are now published.

PROGRESS, RESULTS, AND DISCUSSION

1. Water column results. We finalized analyses of our extensive sampling campaign of the water column along the entire Barents Sea-Svalbard margin in August-September 2015. These data, which include concentrations, isotope measurements and methane oxidation rates document the significance of methane release at the upper limit of gas hydrate stability relative to additional sources on the shelf. Preliminary results were presented at the 2016 Gordon Research Conference on Natural Gas Hydrate (Galveston, TX, March 2016) and a manuscript has been submitted for publication to "Scientific Reports", also published by the Nature consortium and has an impact factor of ~5. The paper is now under review, abstract is attached.
2. Geochemistry: Data from a series of cores recovered at on the fan of Storfjordrenna, west Barents Sea documents recovery of gas hydrate at ~ 0.82 mbsf. indicate that the increase in methane flux inferred sulfate profile, may be linked to an enhanced gas hydrate dissociation in this area. Ongoing studies are aimed at testing this postulate, with the aim to bridge the gap between hydroacoustic flare detection in the water column and the mapping of hydrate reservoir at depth, and provide additional clues to unravel the complex interactions among ice, ocean, microbiology and climate and their sensitivity to both natural and anthropogenic change in Arctic regions. We presented these results at the Gordon Conference on Natural Gas Hydrates March, 2016. A manuscript on these observations entitled "The on-off switch for shallow water Arctic gas hydrate reservoirs" was submitted to Nature Communications, and the editors sent it for formal peer review June 15, 2016. Additional analysis of those fluids is underway. We now completed analyses of major and minor ions as well as some selected Sr isotope data, which suggest a complex system with various fluid sources and advective flow regimes. More analyses are cur-

rently being conducted. Preliminary results will be presented at a Gas In Marine Sediments conference to be held in Tromsø, September 2016. Abstract is attached.

3. **Microbiology.** Marine sediment samples obtained from gas seep sites offshore Svalbard (Barents Sea) were incubated in sterile anoxic seawater media at in situ temperatures and pressures at two different methane partial pressures (0.2 MPa; and 3.8 MPa, at methane saturation). Sediments were sampled after 7, 25, and 129 days. Preliminary data from these experiments were presented at the 2016 Gordon Research Conference on Natural Gas Hydrate (Galveston, TX, March 2016). There were, however, some contamination issues with the sequencing work. We are taking advantage of another expedition to the margin, in which doctoral student Scott Klasek (funded by this grant) is participating to collect additional samples for microbiology, guided by ROV sampling. These new samples will complement the data at hand and serve to remedy some of the issues from contamination problems.
4. **MeBo Expedition:** Torres traveled to Germany and met with G. Bohrmann (chief scientists for upcoming MeBo expedition), to plan details of the collaborative program. Sampling supplies were shipped to Germany, and will be transported with all the equipment to the vessel (M.S. Merian). Geochemical sampling and analyses onboard will be coordinated by WeiLi Hong and Joel Johnson, and samples will be shipped to OSU immediately after the cruise for analyses.
5. **Modeling-** There are now two papers published in which we present an approximate or reduced model of methane hydrate evolution in subsea sediments under conditions of variable salinity. We describe a two-phase three-component physical model. The model is rich enough to allow the study complex dynamics of hydrate formation under the conditions of variable salinity such, and yet is robust and very efficient compared to the published comprehensive fully implicit approaches. In particular, we discuss in detail how the thermodynamics constraints are incorporated in the model and calibrated using experimental data. Copies of the papers are attached.

PROBLEMS OR DELAYS

Some problems were encountered with contamination of enriched samples for microbiology. We secured a place for Scott to sail on another expedition to Svalbard (June 2016), in which additional samples will be collected.

PRODUCTS

- Two papers published on numerical model aspects of the project (attached). Full citations:
Peszyńska, M., Medina, F.P., Hong, W.L. and Torres, M.E., 2015. Reduced Numerical Model for Methane Hydrate Formation under Conditions of Variable Salinity. Time-Stepping Variants and Sensitivity. *Computation*, 4(1), p.1.

Peszynska, M., Hong, W.L. Torres, M.E., and Kim, J-H., 2015. Methane Hydrate Formation in Ullung Basin Under Conditions of Variable Salinity: Reduced Model and Experiments. Transport Porous Media DOI 10.1007/s11242-016-0706-y

- Paper submitted to Scientific Reports June 2016 (abstract attached)
Mau, S. Roemer, M, Torres, M. et al. 2016. Widespread methane seepage along the continental margin off Svalbard - from Bjørnøya to Kongsfjorden
- Paper submitted to Nature Communications June 2016 (abstract attached)
Hong W-L, Torres, M. et al., 2016. The on-off switch for shallow water Arctic gas hydrate reservoirs
- Abstract submitted to Gas in Marine Sediments Conference (attached)
Hong W-L, Torres M. et al., 2016. Fluid geochemistry from a shallow water gas hydrate pingo field south of Svalbard: The role of gas hydrate in fluid transport

Article

Reduced Numerical Model for Methane Hydrate Formation under Conditions of Variable Salinity. Time-Stepping Variants and Sensitivity

Malgorzata Peszynska ^{1,*}, Francis Patricia Medina ^{1,†}, Wei-Li Hong ^{2,3,†} and Marta E. Torres ^{2,†}

Received: 28 November 2015; Accepted: 18 December 2015; Published: 24 December 2015

Academic Editors: Qinjun Kang and Li Chen

¹ Department of Mathematics, Oregon State University, Corvallis, OR 97331, USA; medinaf@science.oregonstate.edu

² College of Earth, Ocean, and Atmospheric Sciences, Oregon State University, Corvallis, OR 97331, USA; wei.l.hung@uit.no (W.-L. H.); mtorres@coas.oregonstate.edu (M.E.T.)

³ CAGE (Centre for Arctic Gas Hydrate, Environment and Climate), Department of Geology, UiT The Arctic University of Norway, Tromsø, Norway

* Correspondence: mpsz@math.oregonstate.edu; Tel.: +1-541-737-9847

† These authors contributed equally to this work.

Abstract: In this paper, we consider a reduced computational model of methane hydrate formation in variable salinity conditions, and give details on the discretization and phase equilibria implementation. We describe three time-stepping variants: Implicit, Semi-implicit, and Sequential, and we compare the accuracy and efficiency of these variants depending on the spatial and temporal discretization parameters. We also study the sensitivity of the model to the simulation parameters and in particular to the reduced phase equilibria model.

Keywords: methane hydrate; multiphase multicomponent flow and transport; reduced computational model; time-stepping; phase equilibria; salinity

MSC: 65M06; 76S05; 76V05; 35R35

1. Introduction

Computational simulation of complex phenomena can provide answers to problems for which no experimental data or theoretical studies are available, but it requires robust, efficient, and accurate numerical models. The problem considered in this paper is of evolution of methane hydrate, which is an ice-like substance present in large amounts in subsea sediments, and which plays an important role both as a potential energy source and environmental hazard as well as in global climate studies [1,2].

In the paper [3] we introduced a reduced model for methane hydrate formation in variable salinity conditions and provided details on the equilibrium phase behavior adapted to a case study from Ulleung Basin. One of the advantages of this reduced model in contrast to fully comprehensive models such as in, e.g., [4], is that the reduced model is easy to implement and to extend, and is amenable to various analyses.

In this paper we describe the computational aspects of the model, with the emphasis placed on the variants of time-stepping. Our reduced model accounts for three components: water, methane, and salt, and two phases: aqueous, and solid (hydrate). Thus, it places in the general framework of multiphase multicomponent models such as those in [5–7] for which accuracy and efficiency have been studied extensively in the past decades. In particular, for the oil-water or black-oil models

described e.g., in [8–13] the best practice is to use mass-conservative spatial schemes combined either with an implicit treatment of pressures and explicit treatment of saturations/concentrations, or with a fully implicit treatment of all phases and components. Typically, the computational complexity of implicit models is the highest, while other variants are easier to implement. In compositional models [14] with M components the pressure solver is complemented with $M-1$ transport equations solved for concentration of the selected $M-1$ species, and followed by flash, *i.e.*, the equilibrium solver. The typical time scales of interest for reservoir simulation with these models are days to decades of production or environmental remediation. On the other hand, in [3] and here we are interested in long-term behavior and hydrate basin modeling, and it makes sense to assume that the pressures and temperatures are known and given by hydrostatic and geothermal distributions. Our models need only to resolve the interdependence between methane and water phase equilibria that depend on the presence of salt, and our time-stepping algorithms have different features than those for the oil-gas reservoir simulators.

We implement the interdependence between the components and phases as follows. The water-methane-salt equilibria are handled using the approach of nonlinear complementarity constraints, and are either tightly or loosely coupled to the salt mass conservation; their implementation is especially easy with the reduced phase behavior model adopted in [3]. We consider and compare three variants of time-stepping that realize these tight or loose couplings: the fully implicit (I), semi-implicit (SI), and sequential (SEQ) algorithms. The comparison that we carry out is intended to demonstrate the merits of these approaches, and guide the choice of a model.

In addition, in this paper we test the sensitivity of the approach to the assumed phase behavior model, as well as to various parameters defining the discretization. The latter is new and was not undertaken for the comprehensive model [4]. It is significant in that it guides the reader in the choice of optimal parameters and shows the robustness of the reduced model.

The paper is organized as follows. In Section 2 we briefly recall the model proposed in [3] including the phase behavior. In Section 3 we describe in detail the time-stepping variants and spatial discretization for that model. In Section 4 we compare the I, SI, and SEQ time-stepping variants, and in Section 5 we discuss the sensitivity of the model to the various parameters of the computational model. We conclude in Section 6.

2. Mathematical Model

In the last decade two classes of models for hydrates have been used to describe hydrate behavior in natural systems. These are the fully comprehensive equilibrium models such as [4], and the simpler conceptual models [2,15,16], in which simplified mechanisms for fluid equilibria and/or kinetics were assumed. The model presented in [3] and discussed here falls somewhere inbetween, and is a direct simplification of the comprehensive model in [4]. The simplicity of the reduced model allows for rigorous mathematical well-posedness analysis in the case of the diffusive transport in [17], and more general analysis in [18] for advective/diffusive transport.

We consider the transport of methane and salt in the sediment reservoir $\Omega \subset \mathbb{R}^d$, $d = 1, 2, 3$. The notation used throughout is provided in Table 1. Each point $x = (x_1, x_2, x_3) \in \Omega$ is at some depth $D(x)$ below the sea surface, with the origin $x = 0$ at the bottom of the Gas Hydrate Stability Zone (GHSZ). At the seafloor, *i.e.*, at the top of the reservoir Ω , we have $x = L$ where L is the thickness of the hydrate zone. Next, at the seafloor, the depth of water above seafloor is the reference depth $D_{ref} = H$, so the sea surface is at $x = L + H$. We also set the coordinate $z = D(x) - D_{ref} = D(x) - H$ measured in mbsf (meters below seafloor) which is used in other models [19]. In the general case of a 2D or 3D reservoir the bathymetry is variable, thus $D(x)$ is measured relative to the (constant) sea surface rather than to the seafloor.

Table 1. Notation and definitions (kg/kg, per kg of liquid phase).

Symbol	Definition	Units/value
Data about reservoir and fluids		
$x = (x_1, x_2, x_3)$	Spatial coordinate	[m]
t	Time variable	[yr]
G	Gravitational acceleration	9.8 m/s ²
$D(x)$	Depth of point x from sea level	[m]
$D_{ref}(x)$	Seafloor depth	[m]
	In 1D case $x = x_3, H = D_{ref}$	
$z = D(x_3) - H$	Depth below seafloor	[m]
(G)HSZ	(Gas) Hydrate stability zone	
P	Pressure	[Pa,MPa]
G_H	Hydrostatic gradient	$\approx 10^4$ Pa/m
T	Temperature	[K]
G_T	Geothermal gradient	[K/m]
q	Darcy volumetric flux of liquid phase	[m/yr]
$D_M = D_S = D^0 S_l \phi_0$	Diffusivity of component C in the liquid phase	[m ² /yr]
	$D^0 = 10^{-9}$ m ² /s = 3×10^{-2} m ² /yr	
ρ_l	Seawater density	1030 kg/m ³
ρ_h	Hydrate density	925 kg/m ³
χ_{hM}	Mass fraction of methane in hydrate phase	0.134 kg/kg
$R = \chi_{hM} \rho_h / \rho_l$	Constant used for methane concentration	0.1203 kg/kg
$\phi_0, \phi = S_l \phi_0$	Porosity in Ω without/with hydrate present	
K_0, K	Permeability in Ω without/with hydrate present	
χ_{IS}^{sw}	Seawater salinity	0.035 [kg/kg]
f_M	Supply of methane (source/sink term)	[kg/kg/yr]
α	Parameter of the reduced model	[kg/kg]
Variables in the model		
$S_l, S_h = 1 - S_l$	Void fraction of liquid and hydrate phases	
χ_{IM}	Mass fraction of methane (solubility) in liquid phase	[kg/kg]
χ_{IS}	Mass fraction of salt (salinity) in liquid phase	[kg/kg]
N_M, N_S	Mass concentration of methane and salt	[kg/kg]

In this paper as in [3] we assume that the conditions in Ω are favorable for hydrate presence and that Ω is entirely within the GHSZ, while the methane is supplied by advection and diffusion from beneath GHSZ. We also assume that $T(x)$ is known and follows the geothermal gradient

$$T(x) = T_{ref} + (D(x) - D_{ref})G_T, \tag{1}$$

where T_{ref} is the temperature at some reference depth D_{ref} and $G_T \approx const$ is the geothermal gradient; see [3] for experimental values. The pressure $P(x)$ is assumed close to the hydrostatic

$$P(x) \approx P_l^0(x) := P_l^0|_{D_{ref}} + \rho_l G(D(x) - D_{ref}) \tag{2}$$

Here P_l^0 is known at the reference depth D_{ref} .

Finally, the actual porosity $\phi(x)$ available to the liquid phase at x is $\phi = \phi_0 S_l$, where S_l is the liquid phase saturation, *i.e.*, void fraction of the liquid phase. The actual permeability $K(x)$ in the presence of hydrate is an important property. However, it is not needed in the 1D model with a constant flux and an assumed hydrostatic pressure distribution.

2.1. Mass Conservation

In region Ω we have the following mass conservation equations for methane and salt components, respectively

$$\frac{\partial \phi_0 N_M}{\partial t} - \nabla \cdot D_M \nabla \chi_{IM} + \nabla \cdot (q \chi_{IM}) = f_M \tag{3a}$$

$$\frac{\partial \phi_0 N_S}{\partial t} - \nabla \cdot D_S \nabla \chi_{IS} + \nabla \cdot (q \chi_{IS}) = 0 \tag{3b}$$

with the definitions

$$N_M = S_l \chi_M + R(1 - S_l), \tag{3c}$$

$$N_S = \chi_{IS} S_l. \tag{3d}$$

where R is given in Table 1. The model is complemented by a pressure equation or q must be given; here we assume the latter. As we explain in [3], the Equation (3) arises as a special case of the first-principles comprehensive model in [4].

We see that in Equation (3) we have two mass conservation Equations (3a,b) with three unknowns that must be chosen from $N_M, N_S, \chi_{IS}, \chi_{IM}$ and S_l . To close the system we use the nonlinear complementarity constraint abbreviated below as [NCC-M] phase constraint. We explain it below.

2.2. Phase Equilibria and [NCC-M] Constraint

The (maximum) amount χ_{IM}^{max} of methane that can be dissolved in the liquid phase depends on the pressure P , temperature T , and the salinity χ_{IS} . Equivalently, these variables determine the circumstances in which $S_l < 1$ and $S_h > 0$, i.e., when the hydrate phase can be present. In addition, χ_{IM}^{max} determines how the total amount of methane N_M is partitioned between the liquid and hydrate phases. This phase equilibrium is expressed concisely as a nonlinear complementarity constraint [NCC-M]

$$\begin{cases} \chi_{IM} \leq \chi_{IM}^{max}, & S_l = 1 \\ \chi_{IM} = \chi_{IM}^{max}, & S_l \leq 1 \\ (\chi_{IM}^{max} - \chi_{IM})(1 - S_l) = 0. \end{cases} \tag{3e}$$

In other words, if $N_M(x, t)$ is small enough so that $N_M < \chi_{IM}^{max}$, then only the liquid phase is present $S_l(x, t) = 1$, and $\chi_{IM} = N_M$ is the independent variable that describes how much methane is dissolved in the liquid. On the other hand, when the amount present $N_M \geq \chi_{IM}^{max}$, the excess amount of methane above χ_{IM}^{max} forms the hydrate phase with $S_h = 1 - S_l > 0$, and $S_l < 1$ becomes the independent variable while $\chi_{IM} = \chi_{IM}^{max}$. This relationship has to be satisfied at every point x, t .

2.2.1. Data for χ_{IM}^{max}

In the hydrate literature [4,20] there are tabulated data, or algebraic models, for how χ_{IM}^{max} depends on P, T, χ_{IS} . In addition, there may be dependence of Equation (3e) on the type of sediment [19,21] but this is out of scope here. In [3] we developed a particular approximation

$$\chi_{IM}^{max} \approx \chi_{IM}^{max}(x, \chi_{IS}) \approx \chi_{IM}^{max,0}(x) + \alpha(x) \chi_{IS}, \tag{4}$$

in which the data $\chi_{IM}^{max,0}(x)$ and $\alpha(x)$ must be provided. This approximation Equation (4) includes as a special case the algebraic model in [19]. In [3] we describe how to obtain $\chi_{IM}^{max,0}(x)$ and $\alpha(x)$ by a fit to the lookup tables extracted from the well known phase equilibrium software CSMGem [22], and we calibrate them for the typical depth, temperature, and salinity conditions found in Ulleung Basin; see [3] and Section 5. As is well known, $\chi_{IM}^{max,0}$ increases with depth, thus decreases

with x . On the other hand, $\alpha(x)$ found with CSMGem is positive while the authors in [23] believe it should be negative; see [3] for details. In Section 5 we discuss the sensitivity of the model to the assumed profile of $\alpha(x)$.

2.2.2. Other Constraints

There are additional constraints that are not part of Equation (3) but are motivated by the physical meaning of the variables S_l, S_h , and χ_{IM} . In particular, we must have $S_h \leq 1$ or

$$S_l \geq 0, \chi_{IM} \geq 0. \tag{5}$$

With some assumptions on χ_{IM}^{max} , the boundary and initial data, and small f_M, q one can prove that Equation (5) holds as a consequence of the maximum principle and other abstract analyses. (See [17] for the diffusive case and [18] for advective and diffusive transport case).

In more general circumstances one cannot prove that Equation (5) holds. In fact, a numerical model may readily produce S_h increasing to 1 and beyond. This clearly is nonphysical, since even before the pores become plugged up and $\phi = S_l \phi_0 = 0$, all the flow and diffusion ceases, local pressures increase, and the sediment may break.

When Equation (5) is violated, a model more general than Equation (3) should be considered. In particular, such a model should include geomechanics and pore-scale effects; see, e.g., the conceptual model described in [21]. However, the analysis of such a model is presently out of scope. In the model discussed in this paper we terminate the simulation when Equation (5) does not hold.

2.3. Boundary and Initial Conditions

The model Equation (3) must be supplemented with appropriate initial conditions imposed on N_M and N_S , and the boundary conditions on the fluxes or on the values of the transport variables χ_{IM} and χ_{IS} . In this paper we set

$$N_M(x, 0) = N_M^0(x), \quad N_S(x, 0) = N_S^0(x), \quad x \in \Omega \tag{6a}$$

$$\chi_{IM}(0, t) = \chi_{IM}^0, \quad \chi_{IM}(L, t) = \chi_{IM}^L = 0, \quad t > 0 \tag{6b}$$

$$\chi_{IS}(0, t) = \chi_{IS}^0, \quad \chi_{IS}(L, t) = \chi_{IS}^L \chi_{IS}^{sw}, \quad t > 0 \tag{6c}$$

The conditions Equation (6c) assign the seawater salinity at $x = L$ and some other salinity χ_{IS}^0 at HSZ known from observations. The conditions Equation (6b) assume some methane present at HSZ $x = 0$, and that there is no methane in the ocean at $x = L$. The choice consistent with Equation (4)

$$\chi_{IM}^0 = \chi_{IM}^{max,0}(0) + \alpha(0)\chi_{IS}^0 \tag{7}$$

allows the maximum possible amount of methane to be transported by advection and diffusion from underneath the HSZ.

3. Numerical Model

Now we provide details of the numerical model for Equation (3). We use mass-conservative spatial discretization based on cell-centered finite differences (FD) with harmonic averaging and a nonuniform structured spatial grid. An alternative discretization of the case $q = 0$, with Finite Elements and mass lumping, was considered in [17], but it would not accommodate large advective fluxes and is not locally mass conservative. For time discretization we use operator splitting: we treat advection explicitly and diffusion implicitly as in [24–26]. The diffusion/equilibria handle two components and are organized in several time-stepping variants. In each variant we have to solve a linear or nonlinear system of equations; for the latter we use Newton (or semismooth Newton) iteration.

After the discretization of Equation (3), at each time step, one solves for the approximate values of the five unknowns $N_M, N_S, \chi_{IM}, \chi_{IS}, S_I$. (At this point we are not yet providing any notation specific to time steps or grid points). Note that Equation (3c) and Equation (3d) are merely the definitions of the terms used in the transport equations Equation (3a), Equation (3b) complemented by the phase equilibria Equation (3e). Thus we can eliminate and actually solve only for three variables $S_I, \chi_{IM}, \chi_{IS}$ the system of three equations which we write as

$$F_M(S_I, \chi_{IM}, \chi_{IS}) = 0 \tag{8a}$$

$$F_S(S_I, \chi_{IM}, \chi_{IS}) = 0 \tag{8b}$$

$$F_{NCC}(S_I, \chi_{IM}, \chi_{IS}) = 0 \tag{8c}$$

The details on discrete form of F_M, F_S , and F_{NCC} which correspond to Equations (3a,b,e), respectively, are developed below. We discuss first the most difficult part of implementing Equation (3e), then we provide details of discretization of the transport equations. The system Equation (8) is nonlinear, and we discuss next the particular variants of the solvers and time-stepping variants.

3.1. Implementing Phase Constraint [NCC-M] in Fully Implicit Models

While it is well known how to discretize and solve advection-diffusion equations, implementing phase equilibria constraint Equation (3e) is challenging. There are practical approaches which have been successfully implemented [4,7]. In addition, approaches known from constrained optimization [27,28] have been recently applied; see [17,29].

In the first class of approaches, the constraint Equation (3e) can be rewritten using the notion of *active/inactive sets* [27]. In this approach at each time step and/or iteration, the (grid) points are identified as either those for which the first part of the inequality Equation (3e) holds, or those where the other complementary inequality must hold. Next, the mass conservation equations are specialized depending on the state of the primary unknowns, and are grouped together and solved for the particular active set of independent unknowns. In summary, in each time step and/or iteration of the nonlinear numerical solver, the solver changes the vector of unknowns depending on which variables need to be used. In consequence, not just the values, but also the sparsity structure of the Jacobian matrix change from iteration to iteration. This approach is known as *variable switching* [4,7] where at each gridpoint one identifies the appropriate independent variable depending on which of the inequalities holds.

In another equivalent approach one takes advantage of the semismooth “min” function as proposed in [29]. We recall that the function “min(u,v)” equals u if $u \leq v$ and v otherwise. We represent Equation (3e) in an equivalent way as

$$\min(\chi_{IM}^{max} - \chi_{IM}, 1 - S_I) = 0. \tag{9}$$

In [17] we showed that the “min” representation of Equation (3e) is equivalent to variable switching discussed above. With the “min” function approach, Equation (9) is a nonlinear equation in the variables χ_{IM} and S_I , and it provides the fifth equation to complement Equations (3a)–(3d) that can be solved together for the five unknowns $N_M, N_S, \chi_{IM}, \chi_{IS}, S_I$.

Since the function “min(u,v)” is piecewise linear and non-differentiable along $u = v$, it is also *semismooth* [28]. The theory of semismooth maps developed in [28] allows us then to analyze the solvability of the resulting nonlinear system of equations.

We found that the approach using Equation (9) is easy to implement and vectorize, and is modular, *i.e.*, it does not require that we rewrite the complex logic of active/inactive sets whenever there is need to expand the logic or the physics in the model. The potential disadvantage of using Equation (9) is that the number of unknowns involved grows from two per grid point to three per

grid point. In practice, however, this has minimal implications on the storage, since all the variables must be stored anyway. On the other hand, the size of the linear system that arises at each iteration when solving Equation (8) is by 50% larger than the size of that with explicit variable switching. However, the matrices in the linear systems corresponding to both approaches are sparse. An efficient implementation of the “min” approach in which sparsity is fixed, can outweigh the cost of the variable switching approach in which the pattern of sparsity varies from iteration to iteration.

3.2. Implementing Phase Constraints in Non-Implicit Models

Some of the time-stepping variants other than fully implicit require local nonlinear solvers called “flash”. These are invoked at each grid point and solve a system simpler than Equation (3e) in which the values of one or more of the variables are assumed known.

Simple flash. The simplest situation is when N_M is known and we know χ_{IM}^{max} . To determine S_l and χ_{IM} we simply use Equations (3e), (3c) to calculate

$$S_l = \frac{N_M - R}{\chi_{IM} - R} = \begin{cases} 1, & N_M \leq \chi_{IM}^{max}(x, t), \\ \frac{N_M - R}{\chi_{IM}^{max}(x, t) - R}, & N_M > \chi_{IM}^{max}(x). \end{cases} \quad (10)$$

Simple flash only is applicable if salinity is fixed because of the dependence of χ_{IM} on χ_{IS} .

Two-variable flash. Given N_M, N_S we can solve for the three unknowns $S_l, \chi_{IM}, \chi_{IS}$ using Equations (3c), (3d) and (9). The implementation is especially easy if Equation (4) is used. This flash solver typically takes 2 or 3 iterations to complete, but may fail when S_h is close to 1.

3.3. Notation in Fully Discrete Model

The notation for discretization is straightforward. We find approximations to the relevant variables at discrete time steps $t_1, t_2, \dots, t_n, \dots$. The transport model Equation (3) advances the model variables from t_n to t_{n+1} , with the time step $\tau = t_{n+1} - t_n$ considered uniform for simplicity. Also for simplicity, we consider the 1D reservoir $\Omega = \cup_i \Omega_i$, where Ω_i are the cells with the centers x_i and uniform length h , and $i = 1, \dots, N_x$. We approximate $N_M(x_i, t_n) \approx N_{M,i}^n$ and set N_M^n to be a vector of $N_{M,i}^n$, with analogous notation applied to other variables.

We start by integrating each of the mass conservation equations over each Ω_i . We show the calculations for methane; the ones for salt are analogous.

Accumulation and source terms. For each i, n we calculate the approximation of accumulation and source terms as follows

$$\int_{\Omega_i} \phi_0 N_M(x, t^n) dx \approx \phi_0(x_i) N_{M,i}^n h. \quad \int_{\Omega_i} f_M(x) dx \approx h f_{M,i}. \quad (11)$$

Advection terms. It suffices to consider only methane advection, since salt advection is treated the same way. We consider first the case $q > 0$. The advective flux

$$\int_{\Omega_i} \nabla \cdot (q \chi_{IM}(x, t^n)) dx \approx q(\chi_{IM,i}^n - \chi_{IM,i-1}^n) \quad (12)$$

is handled by upwinding. Close to the inflow boundary at $i = 1$, we set $\chi_{IM,0}^n$ to the boundary value χ_{IM}^0 . If $q < 0$, we replace the right hand side by $\chi_{IM,i+1}^n - q \chi_{IM,i}^n$, and use the boundary condition χ_{IM}^L on top of the reservoir.

Diffusion terms. For the spatially dependent diffusion coefficient $D_M(x)$ and the variable $\chi_{IM}(x)$ we have, in a standard way [30,31]

$$-\int_{\Omega_i} \nabla \cdot D_M \nabla \chi_{IM} dx \approx -h \left(\frac{D_{M,i+1/2}(\chi_{IM,i+1} - \chi_{IM,i}) - D_{M,i-1/2}(\chi_{IM,i} - \chi_{IM,i-1})}{h^2} \right) \quad (13)$$

where $D_{M,i+1/2}$, $D_{M,i-1/2}$ are found by harmonic averaging of the values $D_{M,i}$, $D_{M,i+1}$ and $D_{M,i}$, $D_{M,i-1}$, respectively. Close to the boundary we apply the discretization described in [32], e.g., at $i = 1$ in place of $\chi_{IM,0}$ we use the boundary value χ_{IM}^0 , with $D_{M,1/2}$ set to $2D_{M,1}$.

We also define the discrete diffusion matrix A with the entries defined so that $h(A\chi_{IM})_i$ is equal to the right hand side of Equation (13). In particular, $A_{ii} = \frac{D_{M,i-1/2} + D_{M,i+1/2}}{h^2}$. With Dirichlet boundary conditions A is symmetric and positive definite, as long as $D > 0$. In 1d A is also tridiagonal. Further, since D_M depends on $\phi_0 S_l$ as in Table 1, the matrix $A = A(S_l)$ depends on the local saturation values. Finally, since $D_M = D_S$ and the type of boundary conditions on χ_{IM} matches that for χ_{IS} , the matrix for salt equation is the same as that for methane.

3.4. Advection Step

The time-stepping variants considered in this paper are explicit in the advection. This allows development of higher-order schemes as well as avoids additional numerical diffusion associated with implicit treatment of advection [24–26]. With this step, we have to consider appropriate boundary conditions which in the operator splitting come from Equations (6b,c); in the advection step we can only impose the boundary condition on the inflow boundary.

In the 1D case considered here $\nabla \cdot q = 0$ implies that q is constant, thus the inflow boundary is determined by the sign of q . If $q > 0$, the inflow boundary is at the bottom of the reservoir at $x = 0$, otherwise it is at $x = L$. In the advection step, we must know χ_{IM} and χ_{IS} on the inflow boundary, and we use here exactly two of Equations (6b,c).

The advection step is as follows. Given N_M^n from previous time step, with the corresponding χ_{IM}^n , we can easily calculate $N_M^{n+1/2}$

$$\frac{\phi_0 N_M^{n+1/2} - \phi_0 N_M^n}{\tau} + \nabla \cdot (q \chi_{IM}^n) = 0 \quad (14a)$$

where the terms $\nabla \cdot$ are approximated by Equation (12). Rearranging Equation (14a) we obtain an explicit expression for the methane amount $\phi_0 N_{M,i}^{n+1/2}$ at the intermediate auxiliary time $t^{n+1/2}$

$$\phi_0 N_{M,i}^{n+1/2} = \phi_0 N_{M,i}^n - \frac{q\tau}{h_i} (\chi_{M,i}^n - \chi_{M,i-1}^n) = 0. \quad (15)$$

As is well known, stability of this explicit advection scheme requires that

$$\frac{|q|\tau}{\phi h} \leq 1 \quad (16)$$

via the well-known Courant-Friedrichs-Lévy (CFL) condition [33] adapted to porous media.

Advection scheme for $N_S^{n+1/2}$ is defined analogously to Equation (15).

3.5. Diffusion Step

Knowing $N_M^{n+1/2}$ and $N_S^{n+1/2}$ from the advection step, we solve the coupled diffusion/phase behavior system for N_M^{n+1} and N_S^{n+1} with the boundary conditions Equations (6b,c). To distinguish between the variants and avoid additional superscripts, we reserve the notation N_M^{n+1} and N_S^{n+1} for the solutions to the fully implicit variant I.

First we recall that with Equation (13) and matrix A we have the vector equation

$$\frac{\phi_0 N_M^{n+1} - \phi_0 N_M^{n+1/2}}{\tau} + A(S_I^n) \chi_{IM}^{n+1} = f_M^{n+1} \tag{17}$$

Note the time lagging of the dependence of matrix A on S_I .

For N_S^{n+1} we have an equation analogous to Equation (17). Additionally, we need to account for [NCC-M]. This coupled system of two component diffusion and phase equilibria is solved with one of the three variants: fully implicit (I), semi-implicit (SI), and sequential (SEQ). See Figure 1 for graphical illustration of the operator splitting and different variants.

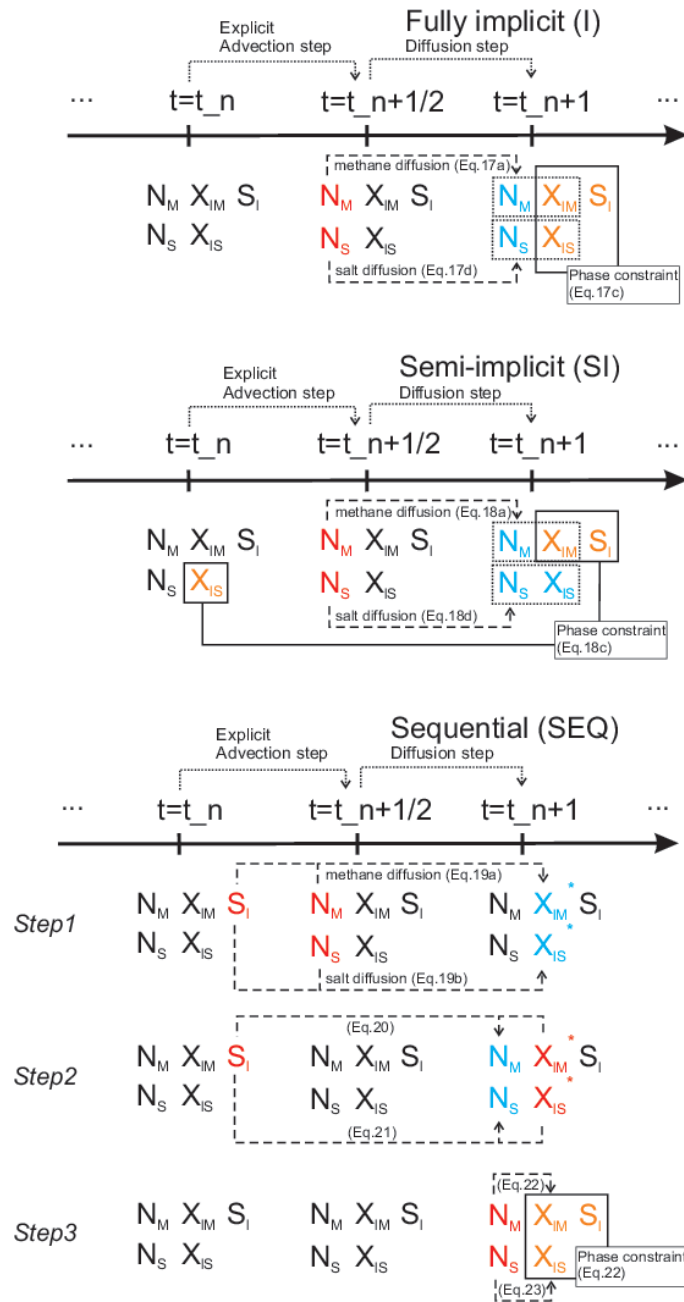


Figure 1. Illustration of time stepping variants.

3.5.1. Variant (I): Fully Implicit

The fully implicit variant solves the coupled two-component diffusion/phase behavior system for $(S_l^{n+1}, \chi_{IM}^{n+1}, \chi_{IS}^{n+1})$ as follows

$$\frac{\phi_0 N_M^{n+1} - \phi_0 N_M^{n+1/2}}{\tau} + A \chi_{IM}^{n+1} = f_M^{n+1}, \tag{18a}$$

$$N_M^{n+1} = S_l^{n+1} \chi_{IM}^{n+1} + R(1 - S_l^{n+1}). \tag{18b}$$

Here Equation (18b) provides the definition of N_M^{n+1} needed in Equation (18a), and is directly implemented in the code. The two unknowns in Equation (18a) are S_l^{n+1} and χ_{IM}^{n+1} ; these are connected to each other via Equations (9) and (4)

$$\min(\chi_{IM}^{max,0}(x) + \alpha(x) \chi_{IS}^{n+1} - \chi_{IM}^{n+1}, 1 - S_l^{n+1}) = 0 \tag{18c}$$

with the dependence on χ_{IS}^{n+1} defined directly by

$$\frac{\phi_0 N_S^{n+1} - \phi_0 N_S^{n+1/2}}{\tau} + A \chi_{IS}^{n+1} = 0 \tag{18d}$$

$$N_S^{n+1} = S_l^{n+1} \chi_{IS}^{n+1} \tag{18e}$$

The Equation (18) is solved using Newton's method for $(S_l^{n+1}, \chi_{IM}^{n+1}, \chi_{IS}^{n+1})$, and the Jacobian of the system is a 3×3 sparse block matrix. Its form and particular pattern of sparsity depend on Equation (18c). Note that in Equation (18) we maintain full consistency of mass conservation between the time steps (up to the tolerance of nonlinear solver), as well as consistency of thermodynamic constraints.

3.5.2. Variant (SI): Semi-Implicit

The semi-implicit variant differs from Equation (18) in the treatment of χ_{IS} in Equation (18c). We time-lag χ_{IS} and remove the two-way coupling between the methane transport and salinity transport. Methane transport in this model is governed by

$$\frac{\widehat{\phi_0 N_M^{n+1}} - \phi_0 N_M^{n+1/2}}{\tau} + A \widehat{\chi_{IM}^{n+1}} = f_M^{n+1}, \tag{19a}$$

$$\widehat{N_M^{n+1}} = \widehat{S_l^{n+1}} \widehat{\chi_{IM}^{n+1}} + R(1 - \widehat{S_l^{n+1}}). \tag{19b}$$

$$\min(\chi_{IM}^{max,0}(x) + \alpha(x) \widehat{\chi_{IS}^n} - \widehat{\chi_{IM}^{n+1}}, 1 - \widehat{S_l^{n+1}}) = 0. \tag{19c}$$

so that these equations are solved for $(\widehat{S_l^{n+1}}, \widehat{\chi_{IM}^{n+1}})$ using Newton's method. The Jacobian of the system is a 2×2 sparse block matrix.

Knowing $\widehat{S_l^{n+1}}$ we can solve the system for $\widehat{\chi_{IS}^{n+1}}$ which is linear

$$\frac{\widehat{\phi_0 N_S^{n+1}} - \phi_0 N_S^{n+1/2}}{\tau} + A \widehat{\chi_{IS}^{n+1}} = 0, \tag{19d}$$

$$\widehat{N_S^{n+1}} = \widehat{S_l^{n+1}} \widehat{\chi_{IS}^{n+1}}. \tag{19e}$$

while the mass conservation between the time steps is enforced in this variant, there is potential inconsistency in thermodynamic constraints introduced by the time-lagging in Equation (19c). To correct this, we follow up with the two-variable local flash solver which corrects the saturations and solubilities while keeping $(\widehat{N_M^{n+1}}, \text{ and } \widehat{N_S^{n+1}})$ fixed.

3.5.3. Variant (SEQ): Sequential

The sequential variant is the simplest to implement and one can easily adapt an existing advection-diffusion code. The advantage of this variant is that each of the global algebraic systems is linear. The disadvantage is that the phase behavior is not fully coupled to the transport dynamics, and fine time-stepping may be needed to ensure accuracy.

The SEQ variant time-lags the saturation variable in the methane and salinity transport equations

$$\frac{\phi_0 \widetilde{S}_l^n \widetilde{\chi}_{IM}^{n+1,*} - \phi_0 N_M^{n+1/2}}{\tau} + A \widetilde{\chi}_{IM}^{n+1,*} = f_M^{n+1} - \frac{\phi R(1 - \widetilde{S}_l^n)}{\tau}, \quad (20a)$$

$$\frac{\phi_0 \widetilde{S}_l^n \widetilde{\chi}_{IS}^{n+1,*} - \phi_0 N_S^{n+1/2}}{\tau} + A \widetilde{\chi}_{IS}^{n+1,*} = 0 \quad (20b)$$

Note that the phase constraint is not imposed in Equation (20), and that the equations are not coupled. We solve them for the temporary unknowns $\widetilde{\chi}_{IM}^{n+1,*}$, $\widetilde{\chi}_{IS}^{n+1,*}$, and next we recalculate the mass concentrations corresponding to the new solubilities from Equations (19b,e)

$$\widetilde{N}_M^{n+1} = \widetilde{S}_l^n \widetilde{\chi}_{IM}^{n+1,*} + R(1 - \widetilde{S}_l^n). \quad (21)$$

$$\widetilde{N}_S^{n+1} = \widetilde{S}_l^n \widetilde{\chi}_{IS}^{n+1,*}. \quad (22)$$

To keep these consistent with Equation (9), we invoke the nonlinear two variable flash solver. Its input are the mass concentrations \widetilde{N}_M^{n+1} , \widetilde{N}_S^{n+1} , and its output are the final new values of solubilities $\widetilde{\chi}_{IM}^{n+1}$, $\widetilde{\chi}_{IS}^{n+1}$, and saturations \widetilde{S}_l^{n+1} which satisfy the discrete version of Equation (9) plus the mass concentration definitions

$$\min(\chi_{IM}^{max,0}(x) + \alpha(x) \widetilde{\chi}_{IS}^{n+1} - \widetilde{\chi}_{IM}^{n+1}, 1 - \widetilde{S}_l^{n+1}) = 0 \quad (23)$$

$$\widetilde{N}_M^{n+1} = \widetilde{S}_l^{n+1} \widetilde{\chi}_{IM}^{n+1} + R(1 - \widetilde{S}_l^{n+1}) \quad (24)$$

$$\widetilde{N}_S^{n+1} = \widetilde{S}_l^{n+1} \widetilde{\chi}_{IS}^{n+1} \quad (25)$$

The flash solver for Equations 23–25 provides the consistency between the mass-related variables and thermodynamic constraints. However, the mass conservation between time steps is not strictly enforced due to time-lagging.

4. Comparison of Performance of the Time Stepping Variants

In this section we evaluate the accuracy, robustness and computational complexity of the proposed I, SI, and SEQ variants of hydrate models using realistic scenarios of methane hydrate formation in typical sediments. We also give details on what time steps appear reasonable, and how to choose discretization parameters.

In oil-gas reservoir simulation the fully implicit algorithms implement directly the backward Euler formula. The fully implicit formulations are usually the most accurate, but also most complex to implement. In turn, sequential and semi-implicit variants are typically less accurate but, at least in principle, they have smaller computational complexity per time step, and are easier to implement than the fully implicit algorithms. Typically, the results of non-implicit schemes converge to those of fully implicit models as $\tau \rightarrow 0$. In fact, non-implicit variants may require small τ in order to resolve, e.g., complicated phase equilibria, heterogeneity, or complex well behavior; the use of small τ somewhat erases the benefits of small computational cost per time step. The non-implicit variants may still have advantages in the easiness of implementation.

The computational experiments we set up to test the variants I, SI, and SEQ are built from the following base case similar to those in [3] for the methane hydrate and salinity conditions in Ulleung Basin.

We set $\Omega = (0, L)$ with $L = 159$ m, and use uniform porosity $\phi = 0.5$. We vary q from large $q = 0.1$ m/yr for which advection dominates, to the case where diffusion is dominant and $q \leq 0.001$ m/yr. We assume that advection and diffusion provide the only transport mechanisms and that $f_M = 0 = f_S$, that is, the only sources of methane are from upward fluxes. For thermodynamics we use the reduced model Equation (4) and [NCC-M] constraint is implemented with Equation (9). Unless otherwise specified, we use the data $\chi_{max}^0(x)$ and $\alpha(x)$ calibrated for Ulleung Basin and shown in [3] and Section 5 with the same boundary and initial conditions. We use zero initial conditions for methane, and assume that the initial distribution of salinities varies linearly between the boundary conditions χ_{IS}^0 and χ_{IS}^M . We run simulations until $T = 10^5$ yr = 100 Kyr, or until S_h reaches the unphysical values close to 1.

Discretization parameters are chosen as follows. We use $N_x = 100$ with $h = 1.59$ in the base case. The time step is subject to the CFL constraint Equation (16). In particular for $q = 0.01$ the largest time step $\tau_{CFL} \approx 78$ yr.

For illustration of the base case in Figure 2 we show the evolution of S_h and χ_{IS} for the case $q = 0.01$ m/yr, with small $\tau = 1$ yr. In this case of strong advective flux the hydrate forms quickly and fills up the domain. These results are similar to those in [3] and more generally to the test cases in [4]. The evolution of salinity shows that there is a boundary layer close to the outflow which forms around $T = 10$ K and remains unchanged afterwards.

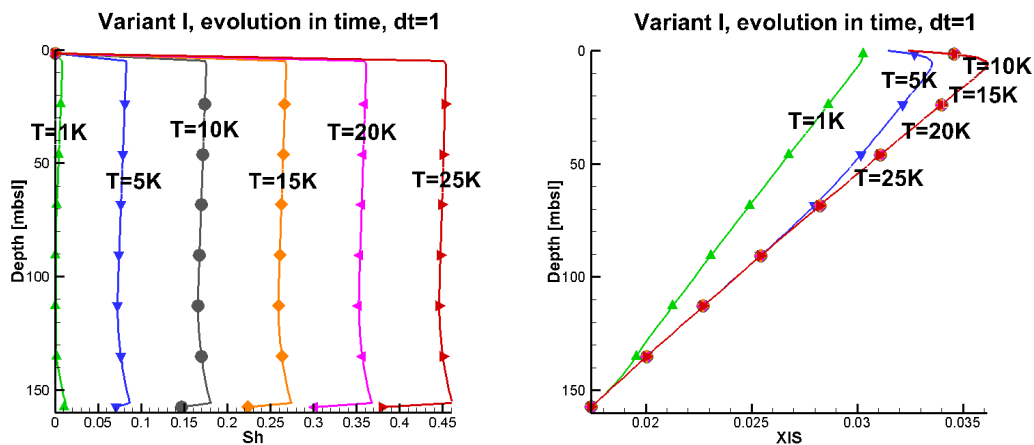


Figure 2. Evolution of hydrate saturation and of salinity for the base case. (left) Plot of S_h , (right) Plot of χ_{IS} . Variable χ_{IM} equals χ_{IM}^{max} at these times and is not shown.

4.1. Accuracy of the Time-Stepping Variants and Choice of Time Step

Here we study the sensitivity to τ which can guide its choice. In general, one wants to use small enough τ obeying the upper bound (16) and such that its further decrease does not have much influence. However, small τ means large number $\frac{T}{\tau}$ of time steps; this is significant in hydrate basin simulations since $\frac{T}{\tau}$ may be easily 10^4 or more. Further, as suggested by our experience from oil-gas reservoir simulations [10,11,13], we expect that for small τ the results of the three variants I, SI, SEQ are very similar, and that for large τ they differ.

In Figure 3 we present the plots of S_h obtained for different τ . Quantitative information supporting these observations is included in Table 2. (We do not present details concerning the evolution of χ_{IS} since the results differ by less than 0.01% in each case.) We notice that the results corresponding to $\tau = 1$ and the variants I, SI, and SEQ are essentially indistinguishable; this degree

of closeness is more than expected. In addition, the results corresponding to the largest advection step $\tau = 78$ and to the variants I, SI and SEQ are close to each other as well; they tend to overpredict those for $\tau = 1$.

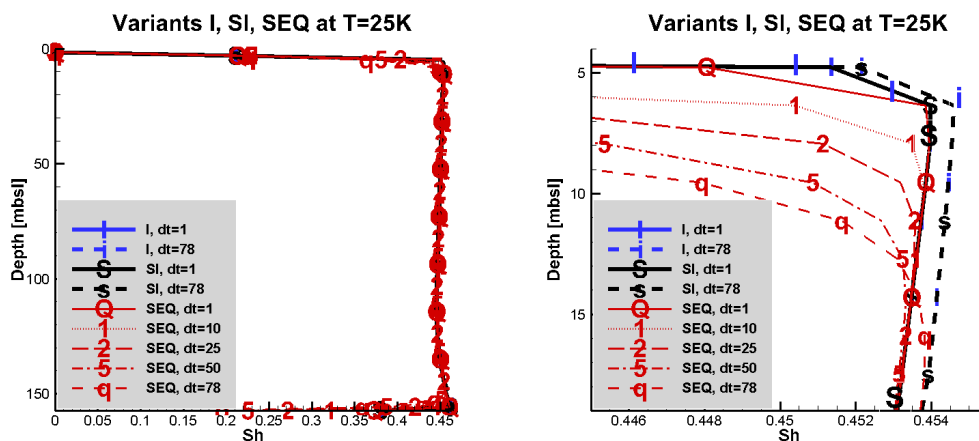


Figure 3. Plots of S_h for different time steps τ (denoted on figure by dt), and different time-stepping variants fully implicit (I), semi-implicit (SI), and sequential (SEQ). (left) Plots over the full range of depth and S_h are essentially indistinguishable. (right) The zoom of the left plot shows a small sensitivity to the choice of time step and of the model variant.

Table 2. Maximum hydrate saturation S_h obtained with different model variants and time steps at $T = 10\text{ K}$ and $T = 25\text{ K}$, all parameters as in base case.

τ	SEQ	SI	I
$T = 10\text{ K}$			
78	0.177208	0.182844	0.182844
70	0.176441	0.181803	0.181803
50	0.176834	0.181267	0.181267
25	0.177841	0.180908	0.180908
10	0.178834	0.180736	0.180736
5	0.179238	0.180688	0.180688
1	0.180183	0.180651	0.180651
$T = 25\text{ K}$			
78	0.456162	0.463925	0.463925
70	0.456803	0.464271	0.464271
50	0.45644	0.462797	0.462797
25	0.457708	0.462438	0.462438
10	0.458886	0.462266	0.462266
5	0.459731	0.462218	0.462218
1	0.460878	0.462181	0.462181

In addition, we see that the model SEQ is potentially the most sensitive of all three to τ close to the boundaries and in areas with larger methane gradients. (This suggests the need for adaptive gridding). In addition, as τ decreases, the results tend to converge to the value for $\tau = 1$. Further decrease of τ (not shown here) does not influence the solution much, thus $\tau = 1$ appears as the smallest sensible choice for this N_x .

4.2. Robustness and Efficiency of the Variants

Above we established that the simulated hydrate saturation values do not seem to significantly depend on the time step τ or on the variant of time stepping. Next we consider the robustness of the

variants and in particular, how they handle difficult physical circumstances such as when S_h is large due to large advective fluxes.

In Table 3 we report on the performance of the nonlinear solver, tested intentionally without any fine-tuning such as line-search. We see that between $T = 25\text{ K}$ and $T = 50\text{ K}$ all variants I, SI, SEQ struggle when $\tau \geq 25$. The model I appears somewhat more robust than the other two and it can simulate the hydrate evolution up to higher values.

Table 3. Robustness of nonlinear solvers depending on the variant and the time step for the simulations of the base case between $T = 25\text{ K}$ and $T = 50\text{ K}$. The robustness is assessed by checking which solver variant is more prone or more robust to failing in the difficult modeling circumstances close to unphysical. We report the critical value S_h^{crit} obtained before the solver fails, and on the number N_{it} of iterations. When N_{it} is denoted by “-”, this means the solver did not complete. For SEQ model, N_{it} denotes the number of flash iterations. For the SI and I models, N_{it} denotes the number of global Newton iterations.

τ	SEQ		SI		I	
	S_h^{crit}	N_{it}	S_h^{crit}	N_{it}	S_h^{crit}	N_{it}
78	0.75833	-	0.767473	-	0.773341	-
70	0.772449	-	0.782752	-	0.781435	-
50	0.806955	-	0.817198	-	0.817198	-
25	0.873396	-	0.880766	-	0.880766	-
10	0.925712	2	0.932267	2	0.932267	3
5	0.926744	2	0.93222	2	0.93222	3

Dependence of the results on q . Next, it is known that the advective fluxes are the hardest physically to handle for hydrate systems, since they provide the source for the fastest hydrate formation.

To test our solvers, we consider the advection-dominated case with large and moderate q , down to the purely diffusive case with $q = 0$. In Figure 4 we present the plots of hydrate saturations at $T = 31\text{ K}$ for different fluxes q . In addition, in Table 4 we report the time T_I when the computational model I predicts that $\max_x S_h(x, T_I) \approx 0.5$. We also report the values T_{SI} and T_{SEQ} also for the variants SI and SEQ.

We see that the variants I and SI report essentially the same values. In fact, a close inspection reveals that the model results differ in less than 0.001% between I and SI for the time steps we used in our implementation. This experiment shows again the robustness of all variants with respect to q , with a slight advantage of the implicit variants.

Computational time and the choice of time step. Finally, we evaluate the computational complexity of the variants, and this is done by comparing the wall clock times for our MATLAB implementation. In order to compare the solvers on equal footing, no additional code vectorization is implemented, but the code takes advantage of the natural MATLAB vector data types. In Table 5 we report the wall clock time.

In general, one expects that for the same time step τ the SEQ model is faster than SI and I, since SEQ only uses global linear solvers and local nonlinear flash routines. However, we see that all solvers require similar amounts of computational time, with a slight advantage of model SI. This may be due to the lack of vectorization applied in local flash routines, while the global linear solvers are naturally vectorized in MATLAB. In addition, the SEQ solver computes more local variables than SI and I.

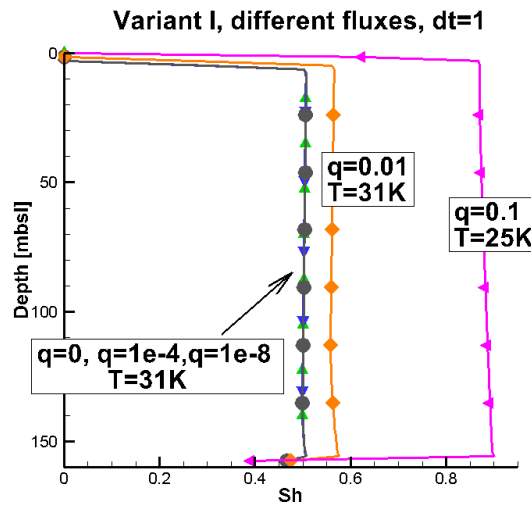


Figure 4. Hydrate saturation at $T = 31\text{ K}$ when different advective fluxes are assumed. For $q = 0.1$ for which high saturation is attained already at $T = 25\text{ K}$ we do not show the plot at $T = 31\text{ K}$.

Table 4. The time T when $\max S_h \approx 0.5$ depending on q , for the base case for each time-stepping variant, respectively, T_I, T_{SI}, T_{SEQ} . Here we use $\tau = 1$.

q	T_I	T_{SI}	T_{SEQ}
0.1	13917	13917	13972
0.01	27014	27014	27091
0.005	28629	28629	28691
0.0001	30568	30568	30587
1e-08	30614	30614	30624

Since with uniform τ the total computational time scales proportionally to the number of time steps, the choice of τ balances the desired accuracy and computational time. For the case considered here it seems that the time step $\tau = 10$ may be the best practical choice.

The efficiency of the solvers may be very different in 2d or 3d simulations, and we intend to report on these in the future.

Table 5. Comparison of computational wall clock time T^w [s] for the three model variants and different time steps, for the base case and $T = 25\text{ K}$.

τ	T_{SEQ}^w	T_{SI}^w	T_I^w
1	591.801	439.806	441.394
10	60.2528	44.0688	47.6352
50	11.8322	8.81442	9.63327
78	7.55206	5.655	6.08011

5. Sensitivity to Physical and Computational Parameters

For a computational model it is crucial to determine what discretization parameters one should use for a given model. In addition, it is important to investigate the sensitivity of the model to the data on $\alpha(x)$ in Equation (4).

Discretization parameters. As the discretization parameters $h, \tau \rightarrow 0$ and the numbers of cells $N_x = \frac{L}{h}$ and time steps increase, it is expected that the numerical solutions of a PDE model converge to the analytical ones in an appropriate sense dictated by the theoretical numerical analysis. The

convergence studies for the purely diffusive one component case of Equation (3) in [17] suggest to vary τ with h either linearly or faster, and to consider various metrics of convergence in appropriate functional spaces. For the present case with significant advection q and variable salinity, we expect the rates to be inferior of the approximate $O(h + \tau)$ rates observed in [17]. The theoretical analysis is underway and will be presented elsewhere.

Here we choose $\tau = O(h)$ and the implicit model; in Figure 5 and Table 6 we present the evidence which confirms that as h decreases, the results seem to converge. At the same time it is obvious that the convergence in saturations is quite rough, as observed earlier in [34].

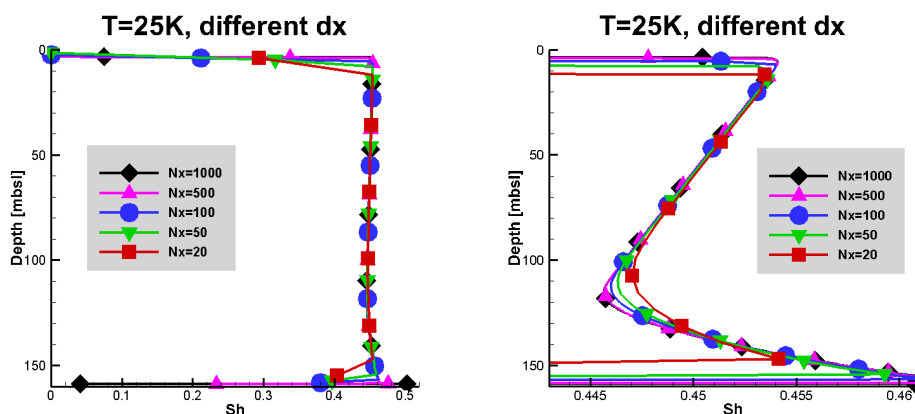


Figure 5. Hydrate saturation for different N_x and h denoted by dx . See Table 6 for the related quantitative information extracted from the simulations.

Table 6. Accuracy and complexity of the computational model depending on N_x , with the time step τ adjusted to vary linearly with h . As the quantity of interest depending on N_x we show the saturation values at $T = 25$ K. This table complements the plots in Figure 5.

N_x	h	τ	$\max S_h$	Wall-Clock Time
10	15.9	10	0.453079	5.6533
25	6.36	4	0.455525	32.644
50	3.18	2	0.459280	121.411
100	1.59	1	0.462181	489.101
200	0.795	0.5	0.465253	2301.53

The question then is what choice of h and τ balance the conflicting need to decrease the computational time as well as to increase the accuracy, while maintaining an adequate model resolution. From the results presented, we suggest that $N_x = 100$ or $N_x = 50$ corresponding to the discretization in space $h \approx 1$ m and in time $\tau \approx 1$ yr are a good choice, since they appear to keep the simulation results within the uncertainty envelope that might not be verifiable experimentally.

However, the sensitivity to τ and h at the boundaries needs to be addressed by a more accurate and adaptive formulation especially if nonhomogeneous sediments and/or additional physics are considered.

Sensitivity to the parameters of the reduced model Equation (4). There is large uncertainty as to what χ_{IM}^{max} one should use. In particular, there may be an error associated with the look-up table process of finding α described in [3] and due to the lack of information on salinity. More broadly, in a comprehensive model χ_{IM}^{max} depends on the unknown pressure and temperature values, and possibly rock type, thus further variability and uncertainty of $\alpha(x)$ should be expected.

We set up therefore test cases to assess this sensitivity. We dub the values of $\alpha(x)$ obtained for Ulleung Basin in [3] the “true” $\alpha_{true}(x)$. Next we simulate the hydrate formation with $\alpha(x) =$

$c\alpha_{\text{true}}(x)$ with $c = 1$, $c = 10$ and $c = -1$. Furthermore, we consider a constant value equal to the average of the true $\alpha(x) = \frac{1}{|\Omega|} \int_{\Omega} \alpha_{\text{true}}(x) dx$, and another $\alpha(x)$ which randomly perturbs $\alpha_{\text{true}}(x)$. The different cases of α are shown in Figure 6, with the corresponding χ_{IM}^{max} which we calculated, for illustration purposes, assuming $\chi_{IS} = \chi_{IS}^{sw}$. In Figure 7 we show the profiles of S_h at $T = 25\text{ K}$ corresponding to the different $\alpha(x)$.

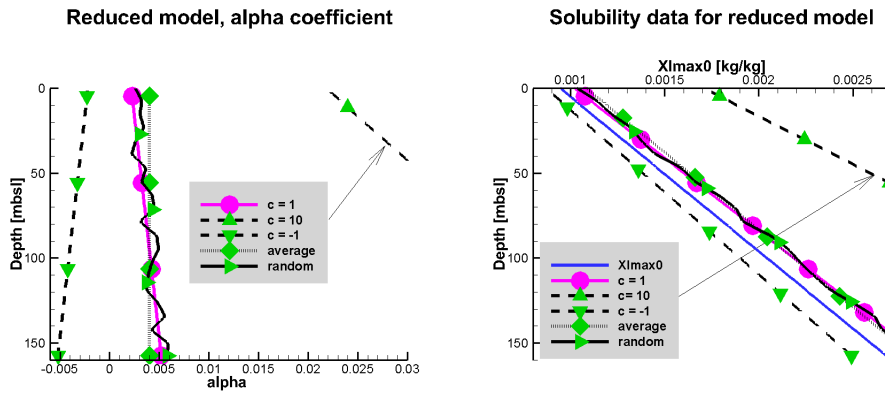


Figure 6. Parameter $\alpha(x)$ as a function of depth used in Section 5 (left) and the corresponding $\chi_{IM}^{max,0}(x)$ computed from Equation (4) and assuming $\chi_{LS} \approx \chi_{IS}^{sw}$ (right). On right the plot of $\chi_{IM}^{max,0}(x)$ is also shown. The base case from Ulleung Basin [3] in both plots is denoted with circles. The other cases correspond to $c = -1$, $c = 10$, the average of $\alpha(x)$, and to a randomly perturbed $\alpha(x)$. The plots for $c = 10$ are out of range and are not fully included.

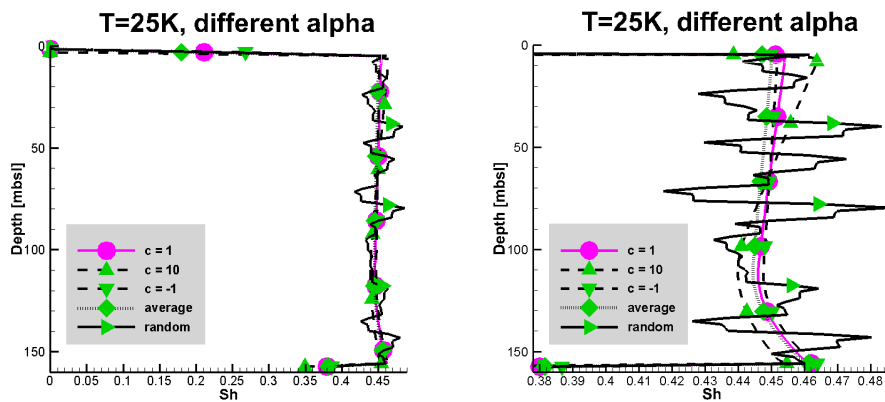


Figure 7. Hydrate saturation for different coefficients α . The figure on the (right) is a zoomed in version of that on the (left).

Comparing the hydrate saturation for $c = -1$ and $c = 10$ shown in Figure 7 to the base case with $c = 1$ we see that since χ_{IM}^{max} is significantly higher when $c = 10$, somewhat less hydrate forms. On the other hand, a randomly perturbed $\alpha(x)$ gives χ_{IM}^{max} with large local variation, and this is reflected in the corresponding hydrate saturation. This significant sensitivity appears to be of qualitative nature, and requires further studies.

6. Conclusions

In this paper we described the details of the discretization and implementation of a reduced methane hydrate model with variable salinity and significant advection proposed in [3]. We carried out several convergence and parameter studies to show that the model is robust and computationally sound. Studies of this type have not been provided for the simplified or the comprehensive implicit

hydrate models from literature, but are crucial to guide the implementation and to inspire further theoretical and algorithmic developments.

In particular, we defined several time stepping variants: implicit I, semi-implicit SI, and sequential SEQ, which were tested and compared using realistic reservoir data from [3]. We found, somewhat surprisingly, that the I and SI variants give almost identical results; this may be explained by only a mild dependence of the model on the salinity variable whose treatment differs in I and SI. Furthermore, in the current implementation and 1d test cases there is no significant advantage in one variant over the others as concerns accuracy, robustness, or efficiency. Still, the I model appears as expected somewhat most robust, while SEQ is the easiest to implement by modifying standard advection-diffusion solvers. We also demonstrated the apparent convergence of the solutions when $h, \tau \rightarrow 0$, and determined practical choices of h, τ . In addition, there is apparent need for grid and model refinement near the boundaries.

Furthermore, we demonstrated the small sensitivity of the reduced thermodynamics model proposed in [3] to the particular value of the coefficient α as long as it is qualitatively close to the one from the reservoir data and is monotone. However, a randomly perturbed and nonmonotone α reveals large sensitivity, and we plan to investigate the reasons further.

Our future work includes theoretical and practical studies of the model convergence as well as its efficiency. There is further need to study additional sets of realistic data and thermodynamics models, and to consider extensions to more complex physical problems.

Acknowledgments: Malgorzata Peszynska and Francis Patricia Medina's research was partially supported by the NSF DMS-1115827 "Hybrid modeling in porous media" and by DMS-1522734 "Phase transitions in porous media across multiple scales". Marta E. Torres and Wei-Li Hong were supported by US Department of Energy grant #DE-FE00135331 and by the Research Council of Norway through its Centres of Excellence funding scheme, project 223259. The authors thank the anonymous reviewers for their comments which helped to improve the manuscript.

Author Contributions: Malgorzata Peszynska, Marta E. Torres and Wei-Li Hong adapted the reduced model to the case study from Ulleung Basin. Malgorzata Peszynska and Wei-Li Hong implemented the reduced model; Malgorzata Peszynska and Francis Patricia Medina set up and tested the numerical model.

Conflicts of Interest: The authors declare no conflict of interest.

References

- Dickens, G.R. Rethinking the global carbon cycle with a large, dynamic and microbially mediated gas hydrate capacitor. *Earth Planet. Sci. Lett.* **2003**, *213*, 169–183.
- Torres, M.; Wallmann, K.; Tréhu, A.; Bohrmann, G.; Borowski, W.; Tomaru, H. Gas hydrate growth, methane transport, and chloride enrichment at the southern summit of Hydrate Ridge, Cascadia margin off Oregon. *Earth Planet. Sci. Lett.* **2004**, *226*, 225–241.
- Peszynska, M.; Hong, W.L.; Torres, M.; Kim, J.H. Methane hydrate formation in Ulleung Basin under conditions of variable salinity. Reduced model and experiments. **2015**, submitted.
- Liu, X.; Flemings, P.B. Dynamic multiphase flow model of hydrate formation in marine sediments. *J. Geophys. Res.* **2007**, *112*, B03101.
- Lake, L.W. *Enhanced Oil Recovery*; Prentice Hall: Upper Saddle River, NJ, USA, 1989.
- Helmig, R. *Multiphase Flow and Transport Processes in the Subsurface*; Springer: Berlin, Germany, 1997.
- Class, H.; Helmig, R. Numerical simulation of non-isothermal multiphase multicomponent processes in porous media 2. Applications for the injection of steam and air. *Adv. Water Resour.* **2002**, *25*, 533–550.
- Trangenstein, J.A.; Bell, J.B. Mathematical structure of the black-oil model for petroleum reservoir simulation. *SIAM J. Appl. Math.* **1989**, *49*, 749–783.
- Chen, Z.; Khlopina, N.L. Degenerate two-phase incompressible flow problems. I. Regularization and numerical results. *Commun. Appl. Anal.* **2001**, *5*, 319–334.
- Lu, Q.; Peszyńska, M.; Wheeler, M.F. A Parallel Multi-Block Black-Oil Model in Multi-Model Implementation. *SPE J.* **2002**, *7*, 278–287.
- Peszyńska, M.; Lu, Q.; Wheeler, M.F. Multiphysics Coupling of Codes. In *Computational Methods in Water Resources*; Balkema: Leiden, The Netherlands, 2000.

12. Wheeler, M.F.; Wheeler, J.A.; Peszyńska, M. A Distributed Computing Portal for Coupling Multi-Physics and Multiple Domains in Porous Media. In *Computational Methods in Water Resources*; Balkema: Leiden, The Netherlands, 2000.
13. Wheeler, M.F.; Peszyńska, M. Computational Engineering and Science Methodologies for Modeling and Simulation of Subsurface Applications. *Adv. Water Resour.* **2002**, *25*, 1147–1173.
14. Coats, K.H.; Thomas, L.K.; Pierson, R.G. Compositional and black oil reservoir simulator. *SPE Reserv. Eval. Eng.* **1995**, *1*, 372–379.
15. Xu, W.; Ruppel, C. Predicting the occurrence, distribution, and evolution of methane hydrate in porous marine sediments. *J. Geophys. Res.* **1999**, *104*, 5081–5095.
16. Nimblett, J.; Ruppel, C. Permeability evolution during the formation of gas hydrates in marine sediments. *J. Geophys. Res.* **2003**, *108*, B9.
17. Gibson, N.L.; Medina, F.P.; Peszynska, M.; Showalter, R.E. Evolution of phase transitions in methane hydrate. *J. Math. Anal. Appl.* **2014**, *409*, 816 – 833.
18. Peszynska, M.; Showalter, R.; Webster, J. Advection of Methane in the Hydrate Zone: Model, Analysis and Examples. *Mathe. Methods Appl. Sci.* **2014**, doi:10.1002/mma.3401.
19. Rempel, A.W. Hydromechanical Processes in Freezing Soils. *Vadose Zone J.* **2012**, *11*, 4.
20. Sloan, E.; Koh, C.A. *Clathrate Hydrates of Natural Gases*, 3rd ed.; CRC Press: Leiden, The Netherlands, 2008.
21. Daigle, H.; Dugan, B. Capillary controls on methane hydrate distribution and fracturing in advective systems. *Geochem. Geophys. Geosyst.* **2011**, *12*, 1–18.
22. Center for Hydrate Research Software CSMHYD and CSMGem. Available online: <http://hydrates.mines.edu/CHR/Software.html> (accessed on 23 December 2015).
23. Zatsepina, O.; Buffett, B. Phase equilibrium of gas hydrate: Implications for the formation of hydrate in the deep sea floor. *Geophys. Res. Lett.* **1997**, *24*, 1567–1570.
24. Dawson, C.N. Godunov-mixed methods for advection-diffusion equations in multidimensions. *SIAM J. Numer. Anal.* **1993**, *30*, 1315–1332.
25. Dawson, C.N.; Wheeler, M.F. Time-splitting methods for advection-diffusion-reaction equations arising in contaminant transport. In Proceedings of the second International Conference on Industrial and Applied Mathematics, Washington, DC, USA, 8–12 July 1991.
26. Wheeler, M.F.; Dawson, C.N. An operator-splitting method for advection-diffusion-reaction problems. In *The Mathematics of Finite Elements and Applications VI*; Whiteman, J.R., Ed.; Academic Press: London, UK, 1987; pp. 463–482.
27. Ito, K.; Kunisch, K. Semi-smooth Newton methods for variational inequalities of the first kind. *M2AN Math. Model. Numer. Anal.* **2003**, *37*, 41–62.
28. Ulbrich, M. *Semismooth Newton Methods for Variational Inequalities and Constrained Optimization Problems in Function Spaces; Vol. 11, MOS-SIAM Series on Optimization*; Society for Industrial and Applied Mathematics (SIAM): Philadelphia, PA, USA, 2011.
29. Gharbia, I.B.; Jaffre, J. Gas phase appearance and disappearance as a problem with complementarity constraints. *Math. Comput. Simul.* **2014**, *99*, 28–36.
30. Peaceman, D.W. *Fundamentals of Numerical Reservoir Simulation*; Elsevier Scientific Publishing Company: Amsterdam, The Netherlands, 1977.
31. Russell, T.F.; Wheeler, M.F. Finite element and finite difference methods for continuous flows in porous media. In *The Mathematics of Reservoir Simulation*; Ewing, R.E., Ed.; SIAM: Philadelphia, PA, USA, 1983.
32. Peszyńska, M.; Jenkins, E.; Wheeler, M.F. Boundary conditions for fully implicit two-phase flow model. In *Recent Advances in Numerical Methods for Partial Differential Equations and Applications*; American Mathematical Soc.: Ann Arbor, MI, USA, 2002.
33. LeVeque, R.J. *Finite Difference Methods for Ordinary and Partial Differential Equations*; Society for Industrial and Applied Mathematics (SIAM): Philadelphia, PA, USA, 2007.
34. Peszyńska, M.; Torres, M.; Tréhu, A. Adaptive modeling of methane hydrates. *Procedia Computer Sci.* **2010**, *1*, 709–717.



Methane Hydrate Formation in Ulleung Basin Under Conditions of Variable Salinity: Reduced Model and Experiments

Malgorzata Peszynska¹ · Wei-Li Hong^{2,3} ·
Marta E. Torres² · Ji-Hoon Kim⁴

Received: 8 June 2015 / Accepted: 3 May 2016

© The Author(s) 2016. This article is published with open access at Springerlink.com

Abstract In this paper, we present a reduced model of methane hydrate formation in variable salinity conditions, with details on the equilibrium phase behavior adapted to a case study from Ulleung Basin. The model simplifies the comprehensive model considered by Liu and Flemings using common assumptions on hydrostatic pressure, geothermal gradient, and phase incompressibility, as well as a simplified phase equilibria model. The two-phase three-component model is very robust and efficient as well as amenable to various numerical analyses, yet is capable of simulating realistic cases. We compare various thermodynamic models for equilibria as well as attempt a quantitative explanation for anomalous spikes of salinity observed in Ulleung Basin.

Keywords Methane hydrate · Flow and transport · Subsea porous sediment · Phase equilibria · Salinity

Mathematics Subject Classification 76S05 · 76V05 · 35R35

M. Peszynska's research was partially supported by the NSF DMS-1115827 "Hybrid modeling in porous media" and by NSF-DMS 1522734 "Phase transitions in porous media across multiple scales". M. E. Torres and W.-L. Hong were supported by US Department of Energy grant #DE-FE00135331 and by the Research Council of Norway through its Centres of Excellence funding scheme, project 223259.

✉ Malgorzata Peszynska
mpesz@math.oregonstate.edu

¹ Department of Mathematics, Oregon State University, Corvallis, OR, USA

² College of Earth, Ocean, and Atmospheric Sciences, Oregon State University, Corvallis, OR, USA

³ Department of Geology, CAGE (Centre for Arctic Gas Hydrate, Environment and Climate), UiT The Arctic University of Norway, Tromsø, Norway

⁴ Petroleum and Marine Research Division, Korea Institute of Geosciences and Mineral Resources (KIGAM), Daejeon, South Korea

1 Introduction

Gas hydrate is a frozen compound in which hydrocarbons are trapped in a water molecule lattice. Gas hydrates comprise a large and dynamic carbon reservoir; see [Milkov et al. \(2004\)](#) and [Dickens \(2003\)](#). In continental margin settings with high methane concentrations, gas hydrates occur naturally in hydrate stability zone, denoted by HSZ, at water depths H greater than 300–500 meters below se level (mbsl), wherever enough methane is present. Numerous laboratory and field studies at gas hydrate-bearing sites, including several drilling expeditions in the past decades, have provided critical background data on the conditions of gas hydrate stability, and have given an overall view of the composition and distribution of gas hydrates in nature. We refer to the recent review ([Collett et al. 2014](#)) and to the monograph ([Sloan and Koh 2008](#)) for an abundant list of references which illustrate the statements above.

Gas hydrate in these systems is known to occur in conditions of extreme variations in salinity. For example, gas hydrate in Ulleung Basin (offshore Korea) occurs in formations with salinities ranging from as low as 22 practical salinity units (psu) to brines with salinity values of 82.4 psu ([Torres et al. 2011](#)). Similar large range in salinity values has been reported in naturally occurring deposits along continental margins ([Torres et al. 2004, 2011](#)). Because of the need to understand methane hydrate evolution, there is growing interest in easy and robust mathematical and computational models which can be calibrated to experimental data and account for, e.g., the variable salinity. This paper is the first of two in which we present an approximate reduced model of methane hydrate evolution in subsea sediments under conditions of variable salinity. Our two-phase three-component physical model is a simplification of comprehensive models in [Liu and Flemings \(2008\)](#), [Garg et al. \(2008\)](#), and [Daigle and Dugan \(2011\)](#) and is simultaneously a significant generalization of the simpler models in [Xu and Ruppel \(1999\)](#), [Nimblett and Ruppel \(2003\)](#), and [Torres et al. \(2004\)](#), in which simplified kinetic or even simpler mechanisms for fluid equilibria were assumed. In contrast to [Torres et al. \(2004\)](#) and consistently with [Liu and Flemings \(2008\)](#), our model fits in the general framework of multiphase multicomponent models such as those in [Lake \(1989\)](#) and [Class et al. \(2002\)](#), and implements bona fide equilibrium phase constraints known from thermodynamics ([Sloan and Koh 2008](#); [Davie et al. 2004](#)), albeit in an approximate manner. In the companion paper [Peszynska et al. \(2016\)](#) we present details of numerical discretization with a particular emphasis on the variants of the time-stepping, which are enabled by the approximations proposed here.

1.1 Model Construction

Our model accounts for both transport modes of methane and of salt: advective and diffusive, and it is derived from that in [Liu and Flemings \(2008\)](#) under the following simplifying assumptions.

- (I) The liquid and hydrate phases are incompressible.
- (II) The pressure is fixed and is close to hydrostatic.
- (III) The temperature gradient is fixed. In particular, the energy equation is not solved and the latent heat is not accounted for.
- (IV) The depth BHSZ of bottom of HSZ is fixed and is determined either from observations, or from phase equilibria using a fixed seawater salinity value. In addition, we consider NaCl as the only inhibitor and ignore the influence of other electrolytes.

After the simplifications, our model is still rich enough to allow the study of complex dynamics of hydrate formation over thousands of years (kyr) under the conditions of variable salinity

and yet is robust and very efficient compared to the published comprehensive approaches. In particular, it solves a system of two mass conservation equations for three variables, of which one is eliminated via an approximate phase equilibrium relationship. This relationship is fixed for the entire simulation, but it allows the two-way coupling between the (transport of) salt and equilibria, and therefore, the model can predict the occurrence of salinity anomalies. In contrast, the comprehensive models available to date solve four equations (mass conservation plus pressure and energy equations) for five variables and must reevaluate the phase equilibria at every grid point, time step, and at every iteration of the nonlinear solver. We acknowledge that due to the simplification following from (I–IV), the model presented here cannot be used when significant pressure or temperature changes occur. Thus, in particular, it is inadequate for simulations of gas production from hydrate.

The crux of our model rests on how the equilibrium phase behavior is formulated. The common approach in fully implicit comprehensive models is to use multivariate lookup tables for the thermodynamics constraints, and to apply variable switching (Class et al. 2002; Liu and Flemings 2008). However, the complexity and sparsity of the phase equilibrium data published in the literature makes the simulation of even simple case studies quite delicate, as we have seen in Peszyńska et al. (2010). Therefore, we use the assumptions (I–IV) and approximate the precise thermodynamics data to formulate a robust, reduced, physically consistent, phase equilibria model. We use the software CSMGem (Sloan and Koh 2008, <http://hydrates.mines.edu/CHR/Software.html>) and compare its results to several empirical and semiempirical algebraic approaches. These comparisons show general consistency but also differences.

Furthermore, we follow our recent work (Gibson et al. 2014; Peszyńska et al. 2015) in which the methane–salinity phase behavior is realized as an (inequality) nonlinear complementarity constraint; we will refer to this elegant explicit construction as NCC-MS. NCC-MS allows to implement easily a range of models from fully comprehensive to the simpler approximate time-stepping variants in which one or more variables are assumed known. With the reduced approximate phase equilibria in the NCC-MS formulation, each part of our model can be carefully analyzed, specialized, tested, and validated, while such an endeavor is nearly impossible in the comprehensive models. In fact, rigorous analysis of the diffusive transport model of methane was first given in Gibson et al. (2014), followed by more general analysis in Peszyńska et al. (2015) for the advective/diffusive transport. The NCC-MS approach enables various variants of numerical discretization and of time-stepping discussed in the second paper Peszyńska et al. (2016).

1.2 Model Application

To demonstrate the application of our model, we choose an extreme example of a site from Ulleung Basin where methane gas is known to migrate through the gas hydrate stability field and gas hydrate is present in near-seafloor sediments characterized by the presence of brine (Torres et al. 2011). We compare the model results with the data from 2010 UBGH2 expedition in which salinity spikes were observed close to the ocean floor (Kim et al. 2013). We use our model to hypothesize on what could have been the dynamics of hydrate formation that can explain these spikes. In accordance with Torres et al. (2011), we argue that large fluxes of dissolved methane cannot explain these anomalies, and the Ulleung Basin data argue against the presence of a high-salinity front as postulated by Liu and Flemings (2006).

The outline of the paper is as follows. We present the model in Sect. 2 and describe how it is calibrated using CSMGem in Sect. 3. In Sect. 4, we describe the setup of simulations and in Sect. 5 compare their results to the experimental data from 2010 UBGH2 expedition,

and discuss the limitations of the current models to explain the salinity spikes. We close in Sect. 6 with conclusions. The “Appendix” provides details on some of the calculations which relate our model to that in Liu and Flemings (2008).

2 Reduced Model of Hydrate and Salinity Transport with Methane Hydrate Formation

We now describe our methane–salt transport model. The notation is summarized in Table 1. The transport takes place in the sediment reservoir Ω under the ocean bottom; $\Omega \subset \mathbb{R}^d$,

Table 1 Notation and definitions

Symbol	Definition	Units/value
$x = (x_1, x_2, x_3)$	Spatial coordinate	(m)
G	Gravitational acceleration	9.8 m/s ²
H	Water depth at seafloor	Model data, (mbsl) ^a
$D_{\text{ref}}(x)$	Reference depth	Model data, (m)
$D(x)$	Depth of point x from sea level	(m)
	In 1D case $x = x_3$, $D_{\text{ref}} = \text{const} = H$	
$z = D(x_3) - H$	Depth below seafloor	(mbsf) ^b
$\phi_0(x)$	porosity of the sediment	Model data
$K_0(x)$	permeability of sediment	Model data, (mD)
ρ_l	Liquid-phase density ^c	1030 kg/m ³
ρ_h	Hydrate-phase density ^c	925 kg/m ³
$G_H = G\rho_l$	Hydrostatic gradient	$\approx 10^4$ Pa/m
G_T	Geothermal gradient	Model data, (K/m)
P_{ref}	Pressure at the reference depth D_{ref}	Model data
T_{ref}	Temperature at the reference depth D_{ref}	Model data
P	Pressure, assumed given ^d ,	(Pa, MPa)
T	Temperature, assumed given ^e	(K)
S_l	Void fraction of liquid phase	
S_h	Void fraction of hydrate phase	
χ_{pC}	Mass fraction of component C in phase p	(kg/kg)
χ_{lM}	Mass fraction (solubility) of methane in liquid phase	(kg/kg)
χ_{lS}, χ_{lS}^m	Mass fraction of salt in liquid phase	(kg/kg), (mol/mol) ^h
$S = 10^{-3} \chi_{lS}$	Salinity	(g/kg)
S^{sw}	Seawater salinity	35 ^f
χ_{hM}	Mass fraction of methane in hydrate phase	0.134 kg/kg
$R = \chi_{hM} \rho_h / \rho_l$	Constant	0.1203 kg/kg
$\chi_{lM}^{\text{max}}(P, T, \chi_{lS})$	Maximum solubility of methane ^g	Model data, (kg/kg)
$\chi_{lM}^{\text{max},0}(x), \alpha(x)$	Data needed for reduced model of χ_{lM}^{max}	

^a Meters below sea level, ^b meters below seafloor, ^c assumed in (I) and (1a), ^d given by (1b), ^e given by (1c), ^f 31 if only NaCl is present, ^g given by phase equilibria model, ^h conversion from (kg/kg) to (mol/mol) is given in Appendix. 1

$d = 1, 2, 3$. Each point $x = (x_1, x_2, x_3) \in \Omega$ is at some depth $D(x)$ below the sea surface. In this paper, we assume that x_3 points in the direction of gravity upwards and that the origin $x = 0$ is somewhere in, or beneath the hydrate reservoir. In the general case of a 3D reservoir, the bathymetry is variable; thus, $D(x)$ is measured relative to the sea surface rather than to the seafloor. In 1D case, $x = x_3$, and it is customary to consider a fixed reference depth $D_{\text{ref}} = H$ equal to the water depth H at seafloor, i.e., at the top of the reservoir.

In this paper, we assume that the conditions in Ω are favorable for hydrate presence: i.e., the pressure is high enough and the temperature is low enough in Ω , and that there is a sufficient methane supply to the system. The latter may result from upward advection of methane gas originating at depth (Torres et al. 2011); methane may also be generated in situ via microbial methanogenesis (Hong et al. 2014). The high-pressure and low-temperature conditions are possible at large depths H , or in Arctic regions. At higher temperatures, such as those occurring at depth within the sediment, methane exist in the gas (“vapor”) phase. Upward methane transport in the gas phase has been documented, but transport in such conditions is not considered in this paper. We refer to the gas phase only when discussing phase equilibria.

The liquid and hydrate phases have respective densities ρ_l, ρ_h which, in general, are mildly dependent on the pressures and temperature, but in our model we assume (I),

$$\rho_l \approx \text{const}, \rho_h \approx \text{const}. \quad (1a)$$

Similar incompressibility assumptions are commonly made in two-phase water–oil reservoir models (Peszyńska et al. 2000; Lu et al. 2002), and (1a) is entirely reasonable over the timescale considered here.

Per assumptions (II) and (III), the pressure $P(x)$ is usually assumed to be close to the hydrostatic pressure, and the temperature usually follows the geothermal gradient

$$P(x) \approx P_{\text{ref}} + G_H(D(x) - D_{\text{ref}}). \quad (1b)$$

$$T(x) = T_{\text{ref}} + G_T(D(x) - D_{\text{ref}}). \quad (1c)$$

The use of (1c) is common (Davie et al. 2004; Rempel 2012); in Peszyńska et al. (2010), we showed little influence of a particular energy model for variable $T(x)$ on methane fluxes over long time period. Instead of (1b), one can find $P(x)$ from the pressure equation defined in the “Appendix.”

The presence of the liquid and hydrate phase is accounted for by their void fractions, S_l, S_h , respectively, also called saturations (Lake 1989; Class et al. 2002). Since $S_l + S_h \equiv 1$, only one of these phase saturations is an independent variable.

The liquid phase (also called “aqueous phase”) consists of water, salt, and dissolved methane components, and their corresponding mass fractions in the liquid phase are denoted by $\chi_{lW}, \chi_{lS}, \chi_{lM}$, respectively. In the hydrate literature, the mass fractions χ_{lM}, χ_{lS} are also called the “solubilities.” The hydrate phase is made of molecules of water and of methane, with the mass fractions denoted by χ_{hW}, χ_{hM} . Because of the physical nature of hydrate crystals built from a fixed proportion of methane and water molecules, it is common to assume the last two are constants, while $\chi_{lW}, \chi_{lS}, \chi_{lM}$ are variables. Since for mass fractions in the same phase we have $\chi_{lW} + \chi_{lS} + \chi_{lM} \equiv 1$ (Lake 1989, 2.2.8a), therefore only two of the variables $\chi_{lW}, \chi_{lM}, \chi_{lS}$ can be independent. In what follows, we choose the salt mass fraction χ_{lS} and one of methane-related variables as the independent variables.

The porosity ϕ_0 and permeability K_0 of sediment typically decrease with overburden pressure, i.e., with increasing $D(x)$. If hydrate is present, then the actual porosity $\phi(x)$ available to the liquid phase is $\phi(x, t) = \phi_0(x)S_l(x, t)$. The actual permeability $K(x)$ in the

presence of hydrate is an important property; however, it is only required when the pressure equation is solved.

2.1 Mass Conservation

In region Ω , we write the mass conservation equations for methane and salt components as in [Liu and Flemings \(2008\)](#). Each equation includes a sum of mass fractions over all phases in which a given component is present. These equations can be derived from first principles as a simplification of the comprehensive model from [Liu and Flemings \(2008\)](#).

$$\frac{\partial \phi_0 N_M}{\partial t} - \nabla \cdot D_M \nabla \chi_{IM} + \nabla \cdot (q \chi_{IM}) = f_M, \quad (2a)$$

$$\frac{\partial \phi_0 N_S}{\partial t} - \nabla \cdot D_S \nabla \chi_{IS} + \nabla \cdot (q \chi_{IS}) = 0. \quad (2b)$$

Here, we have denoted by N_S and N_M the (nondimensional) concentrations of methane and salt relative to water density

$$N_M = S_1 \chi_{IM} + R(1 - S_1), \quad (2c)$$

$$N_S = \chi_{IS} S_1. \quad (2d)$$

where R is a positive constant made precise below.

The flux q is the volumetric Darcy flux of the liquid phase assumed known, and the source term f_M is given. The diffusivities D_M , D_S are functions of S_1

$$D_C = D_C^0 \phi = D_C^0 \phi_0 S_1, \quad (2e)$$

where D_C^0 is the (molecular) diffusivity of the component C in bulk brine, and $\phi_0 S_1$ accounts for the decrease in solubility due to the presence of porous medium ([Lake 1989](#), 2.2–20). For components with (small) molecules of similar size, $D_C^0 \approx D^0 = 10^{-9} \text{m}^2/\text{s}$. We note that more complicated formulas for D_C involving, e.g., tortuosity, and Archie's exponent, can be found, e.g., in [Bear and Cheng \(2010\)](#), Sect. 7.1C and [Dullien \(1979\)](#), Sect. 6.2.4.

In (2), we have four equations and five unknowns: N_M , N_S , χ_{IS} , χ_{IM} and S_1 . After we eliminate N_M , N_S using (2c) and (2d), we have the two mass conservation equations (2a) and (2b) with three unknowns. The additional relationship which closes the system is the phase constraint.

The quantity χ_{IM}^{\max} determines how the methane N_M is partitioned between the liquid and hydrate phases. If $N_M(x, t) < \chi_{IM}^{\max}$, then only the liquid phase is present, i.e., $S_1(x, t) = 1$, $N_M = \chi_{IM}$, and χ_{IM} is the independent variable which describes how much methane is dissolved in the liquid. On the other hand, when the amount present reaches the maximum amount that can be dissolved, i.e., $N_M \geq \chi_{IM}^{\max}$, the excess forms the hydrate phase with $S_h = 1 - S_1 > 0$. In this case, S_1 becomes the independent variable while $\chi_{IM} = \chi_{IM}^{\max}$ fixed.

These constraints can be written concisely as a nonlinear complementarity constraint referred to as NCC-MS

$$\begin{cases} \chi_{IM} \leq \chi_{IM}^{\max}, & S_1 = 1, \\ \chi_{IM} = \chi_{IM}^{\max}, & S_1 \leq 1, \\ (\chi_{IM}^{\max} - \chi_{IM})(1 - S_1) = 0 \end{cases} \quad (2f)$$

The companion paper [Peszynska et al. \(2016\)](#) gives details on how (2f) is implemented in the numerical solver. Below, we discuss the data for χ_{LM}^{\max} .

The model (2) must be supplemented with boundary and initial conditions appropriate to a given case study.

2.2 Phase Behavior: Solubility Constraints

From the hydrate literature [Liu and Flemings \(2008\)](#) and [Sloan and Koh \(2008\)](#), it is known that *maximum solubility constraint* $\chi_{\text{IM}}^{\text{max}}$ depends on P , T , χ_{IS}

$$\chi_{\text{IM}}^{\text{max}} = \chi_{\text{IM}}^{\text{max}}(P, T, \chi_{\text{IS}}), \quad (3)$$

and there are tabulated data, or complex thermodynamics models, for $\chi_{\text{IM}}^{\text{max}}$. Conversely, the variables P , T , χ_{IS} determine the circumstances in which $S_l < 1$ and $S_h > 0$, i.e., when the hydrate phase can be present. The dependence of $\chi_{\text{IM}}^{\text{max}}$ on the type of sediment from [Daigle and Dugan \(2011\)](#) will not be discussed here.

Per assumption (IV), we consider a particular approximation to (3)

$$\chi_{\text{IM}}^{\text{max}} \approx \chi_{\text{IM}}^{\text{max}}(x, \chi_{\text{IS}}) \approx \chi_{\text{IM}}^{\text{max},0}(x) + \alpha(x)\chi_{\text{IS}}, \quad (4)$$

calibrated for the case study in Ulleung Basin. To find $\chi_{\text{IM}}^{\text{max},0}(x)$ and $\alpha(x)$, we use thermodynamics models and data from the literature.

2.3 Numerical Model

The numerical model corresponding to (2) is based on a nonuniform structured grid in 1D and 2D/3D. Discretization is cell-centered finite differences (FD) with harmonic averaging and upwinding. We use operator splitting and treat advection explicitly and diffusion/equilibria implicitly, in several variants of time-stepping applied to the coupled methane–salt system. Details and sensitivity studies are provided in the companion paper [Peszynska et al. \(2016\)](#).

3 Model Calibration

In order to apply the model (2) to realistic cases, we need data, in particular, for $\chi_{\text{IM}}^{\text{max}}$ in (2f). In comprehensive models such as [Liu and Flemings \(2008\)](#), the data for $\chi_{\text{IM}}^{\text{max}}$ are provided via multivariate lookup tables based on sparse data. The sparsity contributes to the roughness of the multivariate sampling, which in turn creates difficulties for a numerical solver. These difficulties can be exacerbated by switching of the primary unknowns as in [Liu and Flemings \(2008\)](#), and by the use of numerical derivatives calculated from multivariate approximations, which can lead to further complications, even if the underlying case study is fairly simple.

In this section, we derive an approximate reduced model (4) for $\chi_{\text{IM}}^{\text{max}}$ which simplifies the phase behavior solver substantially but which honors the well-known qualitative properties of $\chi_{\text{IM}}^{\text{max}}$. In particular, it is known that the values of $\chi_{\text{IM}}^{\text{max}}$ in HSZ are most strongly controlled by the temperature ([Rempel 2012](#); [Davie et al. 2004](#)), with only a mild dependence on salinity, and with negligible dependence on the pressure.

We also compare various theoretical and experimental approaches to provide the context for our approximation. As one of the approaches, we consider the tabulated results of CSMGem. The code CSMGem was developed by [Sloan and Koh \(2008\)](#), <http://hydrates.mines.edu/CHR/Software.html> and calculates $\chi_{\text{IM}}^{\text{max}}$, also called methane hydrate saturation, based on the statistical thermodynamics models proposed in [Barrer and Stuart \(1957\)](#), [Platteeuw and Waals \(1959\)](#), and [Ballard \(2002\)](#). CSMGem is an extension of CSMHYD which is publicly available <http://hydrates.mines.edu/CHR/Software.html>. Since this model is most

detailed, and up to date, we select it for our numerical simulations in Sect. 4. We provide comparisons with the model by Tishchenko et al. (2005) which uses a semiempirical approach based on the theoretical work from Pitzer (1991) to derive $\chi_{\text{IM}}^{\text{max}}$ in conditions for $\chi_{\text{IS}} = 0$ (freshwater) to $\chi_{\text{IS}} = 2\chi_{\text{IS}}^{\text{sw}}$ (twice of seawater salinity). We also consider available experimental data. Some models for $\chi_{\text{IM}}^{\text{max}}$ require the knowledge of methane hydrate stability pressure P_{eq} . We note that in the literature, $\chi_{\text{IM}}^{\text{max}}$ is frequently called MHSAT, and P_{eq} is called MHEQ; we use these symbols in figures.

In practice, to get a model for $\chi_{\text{IM}}^{\text{max}}$, we first determine the HSZ where hydrate can coexist with liquid phase. Our main simplifying assumption (IV) is that the salinity at large depths is close to the seawater value as suggested in Davie et al. (2004). With this, we calculate the pressure P_{eq} at the three-phase equilibrium (aqueous–hydrate–vapor). The knowledge of P_{eq} fixes the depth BHSZ of the bottom of HSZ. Alternatively, as was done for Ulleung Basin, we determine BHSZ from seismic-inferred observations.

Next, above BHSZ, we only consider the two-phase aqueous–hydrate equilibria, and for this, we prepare (offline) the tabulated data on $\chi_{\text{IM}}^{\text{max}}$ depending on (T, P, χ_{IS}) within the range realistic for Ulleung Basin. We recognize that in some settings within the Ulleung Basin and elsewhere, there is evidence for methane transport in the gas phase within the HSZ. In this paper, however, we do not consider the gas transport. The presence of gas phase within the HSZ is the exception, and in most systems, there is no gas within the HSZ.

In general, the data for $\chi_{\text{IM}}^{\text{max}}(T, P, \chi_{\text{IS}})$ are trivariate. However, we can simplify further, since for a given position x within HSZ, we recall that $T(x), P(x)$ are known. In the end, our reduced model is a fit to (4) of the tabulated data against χ_{IS} .

In this paper, we consider the stability and saturation of only structure I (sI) hydrate, with methane as the only guest component in the clathrate structure. Also, as included in assumption (IV), we consider NaCl as the only thermodynamic inhibitor. More generally, other electrolytes such as KCl or CaCl_2 also serve as inhibitors (Sloan and Koh 2008; Dholabhai et al. 1991); however, their effect is by an order of magnitude smaller than that of NaCl and will be neglected.

3.1 Calculation of P_{eq}

The equilibrium pressure P_{eq} is the pressure at which the three phases: liquid, hydrate, and vapor, can coexist. In general, P_{eq} increases with the temperature T and decreases with the salinity χ_{IS} .

Various estimates of the dependence of P_{eq} on T and χ_{IS} are shown in Fig. 1 including those from CSMGem, Maekawa et al. (1995), and Tishchenko et al. (2005). The model for $P_{\text{eq}}(T, \chi_{\text{IS}})$ from CSMGem is obtained by running CSMGem for tabulated values of T, χ_{IS} .

The algebraic model for P_{eq} from Maekawa et al. (1995) is obtained by fitting the laboratory measurements of P_{eq} with the following relationship

$$\ln\left(\frac{P_{\text{eq}}}{P_0}\right) = -926.815 + \frac{31979.3}{T} + 144.909 \ln(T) + 5847.92\chi_{\text{IS}}^{\text{m}} + 322.026(\chi_{\text{IS}}^{\text{m}})^2 + 5840.5 \ln(1 - \chi_{\text{IS}}^{\text{m}}). \quad (5)$$

Here, P_{eq} (MPa), T (K), and $P_0 = 0.101$ MPa are the atmospheric pressures, and $\chi_{\text{IS}}^{\text{m}}$ (mol/mol) is the mole fraction of NaCl in the aqueous phase. The relationship (5) is valid in conditions with salinity up to ~ 8.5 times higher than seawater value and is in good agreement with laboratory data obtained under high-salinity conditions (Roo et al. 1983; Kobayashi et al. 1951).

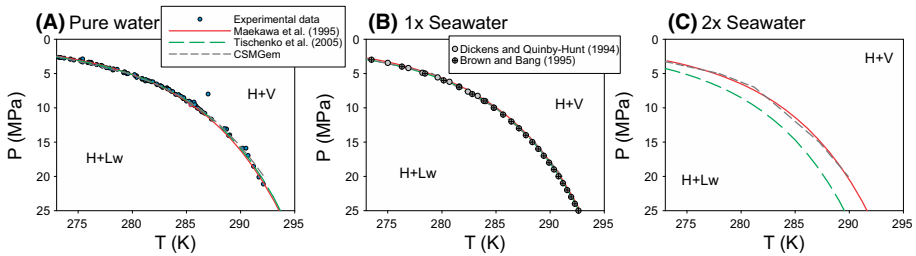


Fig. 1 Methane hydrate stability P_{eq} denoted by MHEQ for different salinity, pressure, and temperature estimated by various models. Available experimental data were shown for comparison. For salinity values below that of seawater, all models agree well with each other and the experimental data. The stability field estimated by Tishchenko et al. (2005) strays away from the theoretical estimation by CSMGem and from the estimation by Maekawa et al. (1995) based on the interpolation of experimental data

As shown in Fig. 1, CSMGem values are close to those given by (5) and to those given by the semiempirical model from Tishchenko et al. (2005). However, for fluids with high salinity, the P_{eq} estimated in Tishchenko et al. (2005) is greater than that estimated by CSMGem and the empirical relationship derived in Maekawa et al. (1995).

However useful and accurate, the model from Maekawa et al. (1995) is not accompanied by a χ_{IM}^{max} model. Thus, in what follows, we use CSMGem as the model for P_{eq} with largest validity range providing both χ_{IM}^{max} and P_{eq} .

3.2 Three-Phase Equilibrium Point(s) and the Depth D_{eq} of BHSZ

The knowledge of D_{eq} and P_{eq} and $T_{eq} = T(x_{eq}(t))$ is needed in the estimates of χ_{IM}^{max} .

From (5), since $T = T(x, t)$ and $\chi_{IS} = \chi_{IS}(x, t)$, we see that $P_{eq} = P_{eq}(x, t)$. If $P = P(x, t)$, then at a given time t there may be a point or points $x = x_{eq}(t)$ at some depth $D_{eq} = D(x_{eq}(t))$ at which

$$x : P(x) = P_{eq}(T(x), \chi_{IS}(x, t)). \tag{6}$$

In general, this means that χ_{IM}^{max} can vary in time t ; this is allowed in the comprehensive models in Liu and Flemings (2006), Liu and Flemings (2008), Peszyńska et al. (2010), and Daigle and Dugan (2011). Further, the depth of points x_{eq} needs not be unique. These considerations must be taken into account when modeling nonhydrostatic pressure, dynamically changing temperature, and in particular when modeling the production of gas from hydrates. Unfortunately, these general considerations also make the numerical model very complex, since a recalculation of P_{eq} and χ_{IM}^{max} must be done at every point, at every time step, and/or even within every iteration of an iterative solver. Furthermore, if χ_{IM}^{max} varies in time, the model is not amenable to even the general mathematical analysis of well-posedness in Peszyńska et al. (2015).

However, in basin modeling, it is reasonable to make some approximations. Following the main assumptions (II, III) we adopted, with hydrostatic pressure and a linear temperature profile as in (1b) and (1c), we see that P, T are monotone in x . If, in addition, the salinity $\chi_{IS} \approx const$, there is at most one such depth D_{eq} where (6) holds; this is the base of HSZ. For depths above D_{eq} (or temperatures lower than T_{eq}), liquid in Ω can coexist with hydrate phase.

If the salinity within HSZ is nonconstant, the conundrum is that we do not know $\chi_{IS}(x)$ when calculating D_{eq} from (6). However, we can assume, as suggested in Davie et al. (2004),

Table 2 Range of validity of P_{eq} and $\chi_{\text{IM}}^{\text{max}}$ models in Sect. 3.3.1

Source	Model	P range (MPa)	T range (K)	S range (g/kg)
Experiments Maekawa et al. (1995)	P_{eq}	$P < 18$	$T < 290$	(0, 20)
Parametric approach Davie et al. (2004)	$\chi_{\text{IM}}^{\text{max}}$	(10, 30)	(273, 300)	(0, S^{sw})
Semiempirical approach Tishchenko et al. (2005)	$P_{\text{eq}}, \chi_{\text{IM}}^{\text{max}}$	$P < 50$	(273, 297)	(0, 70)
CSMGem Sloan and Koh (2008)	$P_{\text{eq}}, \chi_{\text{IM}}^{\text{max}}$	$P < 100^{\text{a}}$	(273, 306) ^b	

^{a,b} Data from [Ballard \(2002\)](#), ^b from Fig. 7.4 in [Ballard \(2002\)](#)

that the salinity at the depths close to D_{eq} equals that of $\chi_{\text{IS}}^{\text{sw}}$. This means that the base D_{eq} of HSZ is calculated only once and is fixed; we identify BHSZ as the set of points x_{eq} for which

$$x_{\text{eq}} : P(x_{\text{eq}}) = P_{\text{eq}}(T(x_{\text{eq}}), \chi_{\text{IS}}^{\text{sw}}). \quad (7a)$$

This approximation is clearly reasonable given the fact that it only determines BHSZ.

Alternatively, one may have additional information about D_{eq} from the seismic-inferred depth of hydrate stability zone. Such was the case of Ulleung Basin where we know the depth of BHSZ (Table 2).

3.3 Model for $\chi_{\text{IM}}^{\text{max}}$

Once we know D_{eq} , the values P_{eq} and T_{eq} are fixed. With these, one calculates the maximum methane mass fraction at the three-phase equilibrium, which is used in turn to get $\chi_{\text{IM}}^{\text{max}}(T(x), \chi_{\text{IS}}(x, t))$ at a given x, t .

We recall first the parametric model from [Davie et al. \(2004\)](#) which provides a linear fit to data generated by the theoretical thermodynamics calculations from [Zatsepin and Buffett \(1997\)](#); see also Table 1 in [Davie et al. \(2004\)](#). The model

$$C_3(T, P) = C_3(T_0, P_0) + \partial_T C_3(T_0, P_0)(T - T_0) + \partial_P C_3(T_0, P_0)(P - P_0), \quad (7b)$$

provides the solubility of methane at the three-phase equilibrium point [Davie et al. \(2004\)](#) based on an estimate of $C_3, \partial_T C_3, \partial_P C_3$ at some given (T_0, P_0) . We provide these for completeness in Table 3.

In particular, knowing $D_{\text{eq}}, P_{\text{eq}}, T_{\text{eq}}$, we can calculate from (7b) the solubility $C_3(T_{\text{eq}}, P_{\text{eq}})$ at the base of HSZ. To correct for the influence of salinity, and to find $\chi_{\text{IM}}^{\text{max}}$ at a given depth $D(x)$ within HSZ, we follow [Davie et al. \(2004\)](#) and use

$$C_{\text{eq}}(T(x), \chi_{\text{IS}}) = C_3(T_{\text{eq}}, P_{\text{eq}}) \exp\left(\frac{T(x) - T_{\text{eq}}}{a}\right) (1 - \beta \chi_{\text{IS}}^{\text{M}}). \quad (7c)$$

Here, $a = 14.4 \text{ K}$, $\beta = 0.1 \text{ mol}^{-1}$ are the parameters determined from the theoretical calculation of ([Zatsepin and Buffett 1997](#)), Eq. (7). The variable $\chi_{\text{IS}}^{\text{rmM}}$ is the salinity in

Table 3 Parameters required in Eq. (7b) to calculate methane hydrate stability and saturation following Davie et al. (2004)

T_0	P_0	α	β	$C_3(T_0, P_0, 0)$	$\partial_T C_3(T_0, P_0, 0)$	$\partial_P C_3(T_0, P_0, 0)$
292 (K)	20 (MPa)	14.4 (°C)	0.1 (mol ⁻¹)	153.36 (mM)	6.34 (mM/K)	1.11 (mM/MPa)

Recall that the unit of C_3 is mM, where M (molarity) is mol/L

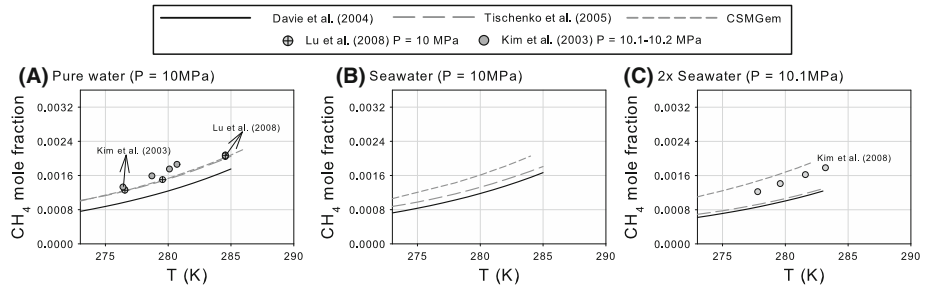


Fig. 2 Methane hydrate saturation χ_{IM}^{max} for different salinity, pressure, and temperature estimated by various models. Note that only few experimental data for pure water and $\chi_{IS} \approx 2\chi_{IS}^{sw}$ are available. The value χ_{IM}^{max} estimated by CSMGem is always higher than the one estimated by Davie et al. Davie et al. (2004), while χ_{IM}^{max} estimated by Tishchenko et al. Tishchenko et al. (2005) overlaps with one or the other approaches. The experimental data are from Lu et al. (2008) and Kim et al. (2003). More figures are available as supplementary material

the unit of molality. See also Rempel (2012, Eq. 11), for (7c) calculated for pure water in heterogeneous sediments. Finally, we obtain χ_{IS}^{max} via the conversion factor

$$\chi_{IM}^{max} \text{ (kg/kg)} = C_{eq} \text{ (mM)} 10^{-3} \frac{16.04}{1030}. \tag{7d}$$

Here, we have used molecular weight of methane equal 16.04 g/mol, the seawater density 1030 g/L, and recalled that 1mM = 10⁻³ mol/L.

Combining (7d) with (7c), we see that the dependence of χ_{IM}^{max} on χ_{IS} is linear, which is consistent with the model postulated in (4).

We compare the model (7d) and various other parametrizations and experiments of χ_{IM}^{max} including CSMGem, (Tishchenko et al. 2005; Sloan and Koh 2008; Davie et al. 2004; Kim et al. 2008) in Fig. 2. Estimates using freshwater and low pressure in Tishchenko et al. (2005) and Sloan and Koh (2008) agree well with each other and with experimental results. As salinity increases, the estimates from both Tishchenko et al. (2005) and Davie et al. (2004) suggest a reduction in χ_{IM}^{max} (i.e., the reduction in the maximum methane mass fraction in equilibrium with hydrate), in agreement with the laboratory results from Kim et al. (2008). CSMGem, however, suggests an increase in χ_{IM}^{max} , consistent with the theoretical calculation of Zatsepina and Buffett (1998), which also suggest an increase in χ_{IM}^{max} at salinities higher than about 0.1 mol/kg of water, or 7 g/kg. Finally, since only few experimental data for high salinity are available (Kim et al. 2008), the evaluation of accuracy of theoretical analyses for high salinity is difficult.

We remark that, if the position D_{eq} of BHSZ changes, one should recalculate C_3 and C_{eq} in (7b) and (7c). This is done in comprehensive models, but has not been included in our model.

3.3.1 Use of CSMGem to Get χ_{IM}^{max}

First, for a given $T(x)$, we calculate P_{eq} . Then, we use $P(x)$ to find the depth D_{eq} of BHSZ assuming seawater salinity at BHSZ. Next, we use CSMGem to estimate χ_{IM}^{max} . We first construct a lookup table in which the input values of pressure P_i , temperature T_j , and salinity $\chi_{IS,k}$ cover the range of interest. For the pressures, we consider the range between the seafloor pressure and that at BHSZ. Since pressure has relatively small effect on χ_{IM}^{max} , we only use these two values $P_1 = P_{ref}$ and $P_2 = P_{BSR}$ as the grid points. The temperature dependence is very significant, and we consider the interval $T_j \in (273 \text{ K}, 291 \text{ K})$, with $\Delta T = 2 \text{ K}$. We also consider salinity values $\chi_{IS,k} \in (0, 0.125) \text{ kg/kg}$, where the right end point is four times the seawater salinity χ_{IS}^{sw} , with $\Delta \chi_{IS} = 0.0156$ for the total of nine grid points.

Next, we use CSMGem to estimate χ_{IM}^{max} for each of the grid points $(P_i, T_j, \chi_{IS,k})$. This is done by trial and error: We provide CSMGem with some guess of χ_{IM} , and CSMGem predicts the phase conditions for $(P_i, T_j, \chi_{IS,k}, \chi_{IM})$. We try different values of χ_{IM} until we locate the maximum methane mass fraction $\chi_{IM}^{max} |_{(P_i, T_j, \chi_{IS,k})}$ for which methane is only in two phases, i.e., as dissolved methane and methane hydrate. This process gives a table of values

$$(P_i, T_j, \chi_{IS,k}, \chi_{IM}^{max} |_{(P_i, T_j, \chi_{IS,k})})$$

with $1 \leq i \leq 2, 1 \leq j \leq 20, 1 \leq k \leq 9$.

Next, for each grid point (P_i, T_j) , we estimate the regression between $\chi_{IS,k}$ and $\chi_{IM}^{max} |_{(P_i, T_j, \chi_{IS,k})}$. The regression provides us, for each (P_i, T_j) in the gridded table, with the coefficients A_{ij} and B_{ij} of the linear model so that

$$\chi_{IM}^{max} |_{(P_i, T_j, \chi_{IS,k})} = A_{ij} + B_{ij} \chi_{IS,k}.$$

As shown in Fig. 3, the values A_{ij}, B_{ij} are not very sensitive to the pressure; thus, we approximate further

$$\chi_{IM}^{max} |_{(P_i, T_j, \chi_{IS,k})} = \bar{A}_j + \bar{B}_j \chi_{IS,k}. \tag{8}$$

where $\bar{A}_j = A_{1j}, \bar{B}_j = B_{1j}$.

For the cases where $P(x), x \in \Omega$ changes by more than 1-2 MPa, one may consider a more accurate multivariate model than (8).

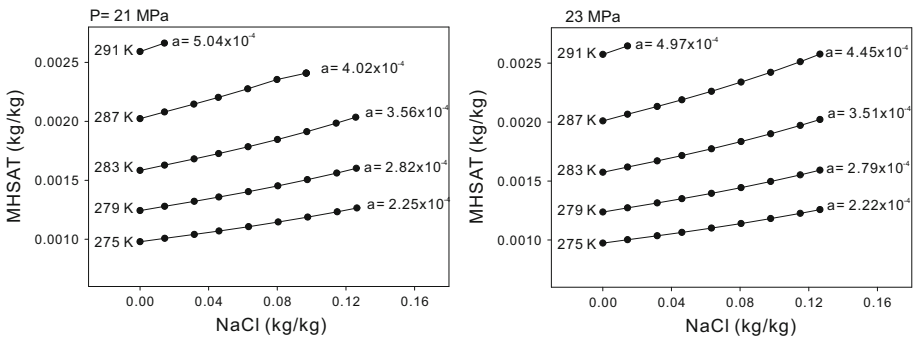


Fig. 3 Dependence of χ_{IM}^{max} on the salinity χ_{IS} estimated from CSMGem as in (9). Positive value of the slope α indicates that the methane hydrate is more difficult to form at higher salinity. Higher temperature elevates χ_{IM}^{max} and makes methane hydrate more difficult to form. χ_{IM}^{max} decreases only slightly when increasing pressure at the same temperature and salinity

In the last step, we connect (8) to the model (4). With constant geothermal gradient according to (1c), each T_j corresponds to a unique depth D_j ; thus, we set up a lookup table extending (8) to

$$\chi_{\text{IM}}^{\text{max}}(x, t) = \bar{A}(D(x)) + \bar{B}(D(x))\chi_{\text{IS}}(x, t) \quad (9)$$

where $\bar{A}(x)$, $\bar{B}(x)$ are the appropriate piecewise linear functions built from (D_j, A_j) and (D_j, B_j) , respectively.

We observe that there is qualitative agreement between the approximation (4), the parametric model (7c), and the regression (9). In particular, $\chi_{\text{IM}}^{\text{max},0}(x) := \bar{A}(D(x))$ is the temperature dependent coefficient, and $\alpha(x) := \bar{B}(D(x))$ is the salinity-dependent coefficient.

However, we note that \bar{B} found from tabulated data can have any sign. In fact, we find that it is positive, in contrast to the model (7c). In the companion paper [Peszynska et al. \(2016\)](#) we discuss the sensitivity of simulations to the particular value and to the sign of \bar{B} .

4 Application to the Ulleung Basin Case

In this section, we describe how the model (2) was calibrated using data from Ulleung Basin. The second drilling expedition to the Ulleung Basin (UBGH2) ([Bahk and Kim 2013](#)) offshore South Korea (Fig. 4) drilled four sites that targeted the acoustic blanking chimneys in the seismic reflection data. These acoustic features extend from below the HSZ to near the seafloor, where they are usually accompanied by the presence of pockmarks or mounds on the seafloor bathymetry ([Horozal et al. 2009](#)). The seismic blanking zones have been interpreted to image conduits for gas migration, because of the low impedance of seismic waves as they travel through gas. Gas hydrates with different modes of occurrence were recovered from all four sites. From three of the sites (UBGH2-3, UBGH2-7, UBGH2-11), massive gas hydrates related to fracture-filling (or grain displacing) morphology were observed at depths shallower than 6 mbsf ([Bahk and Kim 2013](#)). Disseminated gas hydrates related to either fracture-filling or pore-filling modes were recovered from UBGH2-2_1 ([Bahk and Kim 2013](#)). Finally, the porosity values were found to be

$$\phi_0 \in (0.6, 0.87), \quad (10)$$

with a few local anomalies down to 0.4. In the simulations, we use the actual nonconstant porosity data for this site.

4.1 Salinity Data

Salinity, pressure, and temperature conditions are fundamental in constraining the stability of gas hydrate. For the Ulleung Basin, the salinity data obtained shipboard are of less precision than dissolved chloride ([Scientists 2010](#)). We therefore use the chloride data and convert it to salinity (see Fig. 5) using the empirical relationship obtained by fitting all data from UBGH2 sites with

$$S = 61.6\text{Cl}_M + 1.4301, \quad (11)$$

where Cl_M (M) is chloride concentration in mol/L (M).

Pore water chloride profiles from these four sites reflect gas hydrate kinetics and fluid origins; see Fig. 5. Chloride concentrations at the bottom of the recovered sections are always lower than seawater, which have been interpreted as reflecting input of freshwater from

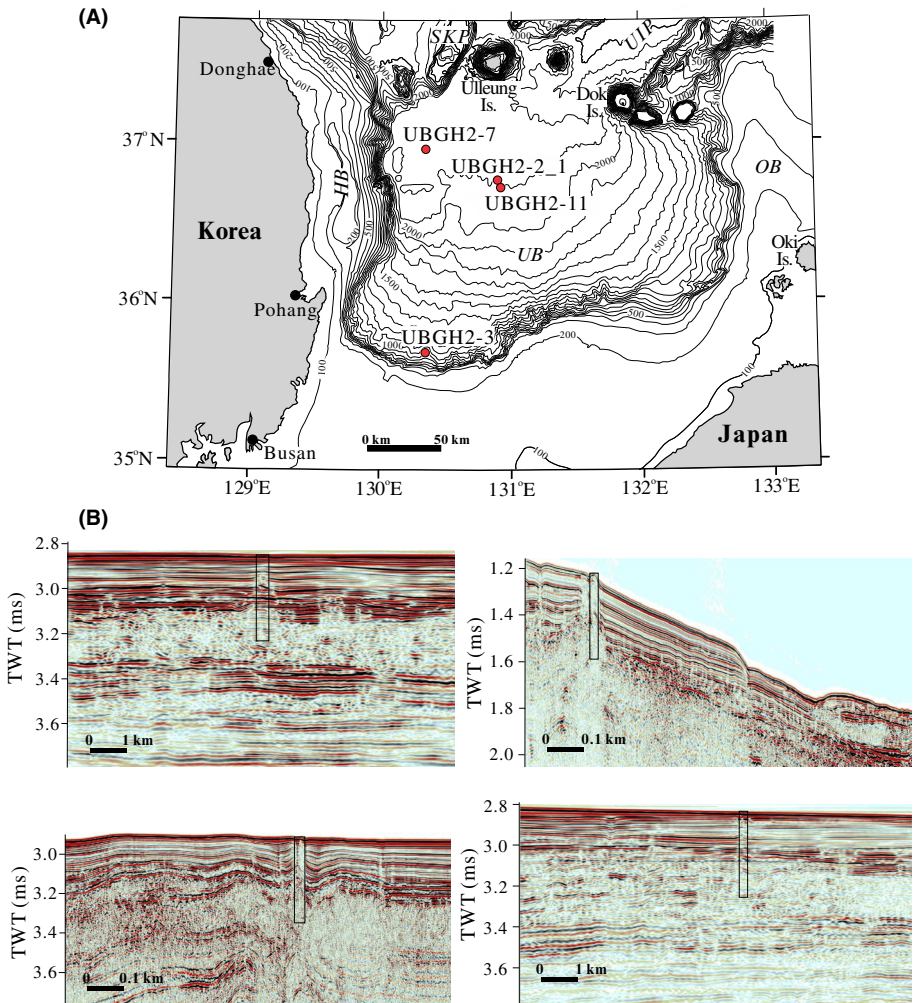


Fig. 4 **a** Bathymetric map of the Ulleung Basin, offshore Korea, showing the location of the four drilled sites in this study. **b** Seismic profiles across the drilled sites. The rectangles are the location and the depth covered by drilling. These locations were chosen inside the seismic blanking zone in the chimneys. (From KIGAM)

clay mineral dehydration reactions at depth (Kim et al. 2013). The shallower sediment sections show different degrees of chloride enrichment at each site. At UBGH2-3, we have the most prominent chloride peak, with concentrations almost three times the seawater value. At UBGH2-11 and UBGH2-7, the enrichments range from a few millimolar to ≈ 180 M above seawater concentration, respectively. The site UBGH2-2_1 shows the strongest signal of deep-sourced freshwater input, but has no enrichments in chloride. It is worth noticing that these enrichments in chloride concentration are minimum values, since they may be affected by gas hydrate dissociation during core recovery (Scientists 2010). We also refer to Malinverno et al. (2008) for more discussion.

Finally, the salinities we infer from shipboard measurements were not measured in situ. Indeed, the “real” Cl and salinity are likely higher than what we measured, because of gas

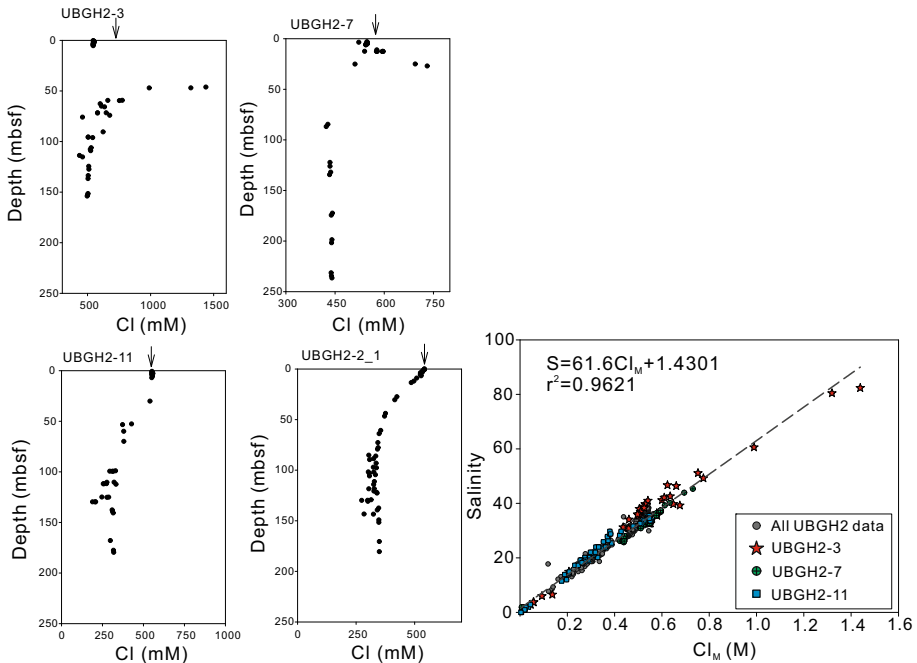


Fig. 5 Left profiles of Cl in pore water for the four study sites. Right empirical relationship between salinity and chlorinity for UBGH2 data. The arrow denotes seawater values. The freshening observed at depth precludes inferences for the presence of a high-salinity front as the mechanism to support methane transport in the gas phase as postulated by Liu and Flemings (2008)

hydrate dissociation during recovery lowers the pore fluid salt and chloride concentrations, but none of our conclusions drawn in Sect. 5 will be different if using the “real” salinity.

4.2 Temperature and Pressure Data

The data from Ulleung Basin include temperature T_{ref} at the seafloor and downhole temperature measurements from which we estimate G_T , see Table 4.

Further, with known hydrostatic gradient G_H , the pressure at the seafloor, the pressure at the first gas hydrate appearance, and the pressure at the base of the HSZ are listed in Table 4. In a typical reservoir of thickness of 100 to 200 m, the pressure difference in the hydrostatic distribution is about $\Delta P_H \leq 2$ MPa, and it significantly exceeds the contributions to pressure difference that may occur due to advective fluxes that have been observed. Thus, it makes sense to assume hydrostatic relationship (1b).

5 Model Results and Discussion

In this section, we apply our model to the case from UBGH2-7 in an effort to illustrate the applicability of the model to a natural system and to explain the coupled methane and salinity dynamics resulting in salinity spikes accompanying hydrate deposits. We provide background with motivation, details on the setup of the cases, and we discuss the results.

Table 4 Basin parameters of the four study sites in Ulleung Basin

	UBGH2-2_1	UBGH2-3	UBGH2-7	UBGH2-11
Seafloor depth $D_{\text{ref}} = H(\text{m})$	2092	898	2145	2082
Pressure P_{ref} (MPa) at seafloor ^a	21.13	9.06	21.65	21.02
Temperature T_{ref} (K) ^b at seafloor	273.35	273.45	273.55	274.35
BHSZ depth (mbsf)	176.0	131.6	124	159
P at BHSZ (MPa) ^a	22.89	10.39	22.90	22.62
T at BHSZ (K) ^c	292.7	286	294.8	292.2
χ_{IS} at BHSZ (kg/kg)	0.0229	0.0323	0.0273	0.0210
FGH depth (mbsf) ^d	76.4	6.2	7	7
P at FGH (MPa) ^a	21.89	9.13	21.71	21.09
T at FGH (K) ^c	281.6	274	274.6	275.1
Geothermal gradient G_{T} (K/m) ^e	0.108	0.095	0.171	0.120

FGH is the depth of first observed hydrate appearance. ^a Pressure was calculated assuming (1b). ^b Seafloor temperature was measured at each of the drilling site Lee et al. (2013). ^c Temperature is estimated from seafloor temperature and geothermal gradient with (1c). ^d The depth of hydrate first appearance was determined by visual observations of hydrate or by pore water anomalies. ^e Geothermal gradient G_{T} determined from linear regression of downhole temperature measurements at all UBGH2 drill sites Riedel et al. (2013)

Background. Based on purely thermodynamic considerations, water and gas hydrate will coexist in the sediment section that lies within the HSZ. As the temperature in the sediment increases according to the attendant geothermal gradient, a depth is reached where gas hydrate becomes unstable. Below this depth, water and free gas coexist, but as long as there is water available in the formation, free gas should not be present within the HSZ. There is however ample evidence of methane migration through the HSZ at gas hydrate provinces worldwide. Observations of methane discharge at the seafloor, pressure core sampling imaging, and analyses of methane concentrations at in situ pressures, acoustic blanking in seismic data, and logging data all support the vertical migration of gas through the HSZ, which in most cases result in the formation of massive gas hydrate deposits at or near the seafloor (Torres et al. 2011).

The report of the presence of near-surface brines associated with massive gas hydrate deposits on Hydrate Ridge (Oregon) led to the development of hypotheses to explain this observation. Torres et al. (2004) used a one-dimensional transient model to simulate the observed chloride enrichment and show that in order to reach the observed high chloride values, methane must be transported in the gas phase from the depth of the BSR to the seafloor. Methane transport exclusively in the dissolved phase is not enough to form methane hydrate at the rates needed to generate the observed chloride enrichment. As shown by Trehu et al. (2004), when enough free gas accumulates below the HSZ, the excess (nonhydrostatic) pressure at the top of the gas layer may be sufficient to fracture the sediments and drive gas toward the seafloor. Alternatively, Liu and Fleming argue in Liu and Flemings (2006) that as gas migrates from below the HSZ, gas hydrate formation depletes water and elevates salinity enough to shift the local three-phase equilibrium to the point where the aqueous water, hydrate, and vapor (free gas) coexist, thus allowing vertical migration of free gas through the HSZ. The role of salinity in the thermodynamics of hydrate is important here, since there is a 1.1 °C offset in dissociation temperature of methane hydrate in 33%NaCl, relative to that

for pure water. Rapid increase in salinity due to recent gas hydrate formation poses negative feedback on hydrate crystallization by shifting the phase boundary.

There have been additional observations of pore fluids highly enriched in dissolved chloride at sites of massive gas hydrate occurrence in northern Cascadia accretionary margin (Canada), the Krishna–Godavari Basin (India), and the Ulleung Basin (Korea). The sites drilled on seismic acoustic chimneys indicative of free gas transport in the Ulleung Basin all show chloride enrichments of up to 1440 mM from near-seafloor to depths of 100 meters below seafloor (mbsf). Below the depth of chloride maxima, however, chloride values approach concentrations that are lower or equal to seawater values, with minor negative chloride anomalies superimposed on baseline that reflect discrete gas hydrate-bearing horizons (Torres et al. 2011). None of these sites, however, show any evidence for the elevated salinity values beneath the shallow lens of massive hydrate formation (Torres et al. 2011). Extreme high-salinity values (of up to 3 times seawater values (Liu and Flemings 2008) have been postulated by current models, as these high values are needed to create a shift in the gas hydrate thermodynamic equilibrium and sustain gas transport from the base of the gas hydrate stability front to the seafloor.

Below we apply our model in an effort to explain the observed salinity anomalies. It turns out that we are only partially successful.

Model setup. We use fully implicit numerical solver implementation of (2) with $dx = 1\text{m}$, $dt = 1\text{year}$; see details in Peszynska et al. (2016).

The data from UBGH2-7 are along the vertical transect, and thus, the case is essentially 1D, and we set up $\Omega = (0, L)$ where $L = 124\text{m}$ is the reservoir thickness. The bottom of the reservoir is at $x = 0$ and is at BHSZ. We assume T and P as in Sect. 4.2. We use relatively small advective flux q , and thus, solving pressure equation is not necessary.

We set up the following boundary and initial conditions. The boundary conditions for methane and salt components are needed at $x = 0$ and $x = L$. For the top of reservoir $x = L$, i.e., sea bottom, we use seawater salinity and zero methane concentrations

$$\chi_{\text{IM}}(L, t) = 0, \quad \chi_{\text{IS}}(L, t) = \chi_{\text{IS}}^{\text{sw}}. \quad (12)$$

At $x = 0$, we assume conditions above BHSZ and set up boundary condition for methane to be given by $\chi_{\text{IM}}^{\text{max}}$ at the corresponding depth. For salinity at $x = 0$, we use the observed salinity values $\chi_{\text{IS}}^0 = 0.0273\text{ kg/kg}$ shown in Fig. 5 following (Kim et al. 2013)

$$\chi_{\text{IM}}(0, t) = \chi_{\text{IM}}^{\text{max}}(0, \chi_{\text{IS}}^0), \quad \chi_{\text{IS}}(0, t) = \chi_{\text{IS}}^0. \quad (13)$$

The initial conditions are

$$\chi_{\text{IM}}(x, 0) = 0, \quad \chi_{\text{IS}}(x, 0) = \chi_{\text{IS}}^I(x), \quad (14)$$

where $\chi_{\text{IS}}^I(x)$ is a linear function between $\chi_{\text{IS}}(0, 0)$ and $\chi_{\text{IS}}(L, 0)$.

We use reservoir parameters listed in Table 4 and set up five different scenarios to investigate how the profiles of dissolved methane concentration, salinity, and gas hydrate saturation respond to different modes of aqueous fluid transport. The cases are summarized in Table 5.

5.1 Scenarios with Different Advection Rates and Sources

Cases 1, 2, and 3 compare simulation scenarios with different Peclet numbers as in Fig. 6, 7, and 8. Advection transports the fluids with abundant methane from sources below HSZ, which facilitates the formation of hydrate, see Fig. 8. With a strong advective flux (Case 3),

Table 5 Parameters of the five simulation cases

Case #	Diffusion rate D^{0a} (m^2/year) ^a	Advection rate q (m/year) ^b	Peclet number	Methane source f_M^c ($\text{kg}/\text{kg}/\text{kyr}$)	Time T (kyr)
1	3×10^{-2}	1.2×10^{-9}	4×10^{-6}	0	25, 50, 100
2	3×10^{-2}	2×10^{-4}	0.83	0	25, 50, 100
3	3×10^{-2}	2×10^{-2}	82.7	0	2.5, 10, 25, 100
4	3×10^{-2}	1×10^{-9}	4×10^{-6}	4×10^{-2}	0.5, 1, 2
5	3×10^{-2}	2×10^{-3}	8.3	4×10^{-2}	0.5, 1, 2

^a Corresponds to the standard molecular diffusivity $10^{-9} \text{m}^2/\text{s}$. ^b 1 m/year corresponds to $\approx 3 \times 10^{-5} \text{mm/s}$. ^c kg of dissolved methane in 1 kg of seawater for every thousand years. Peclet number $Pe = qL/D$ where $L = 124 \text{m}$ is the reservoir depth

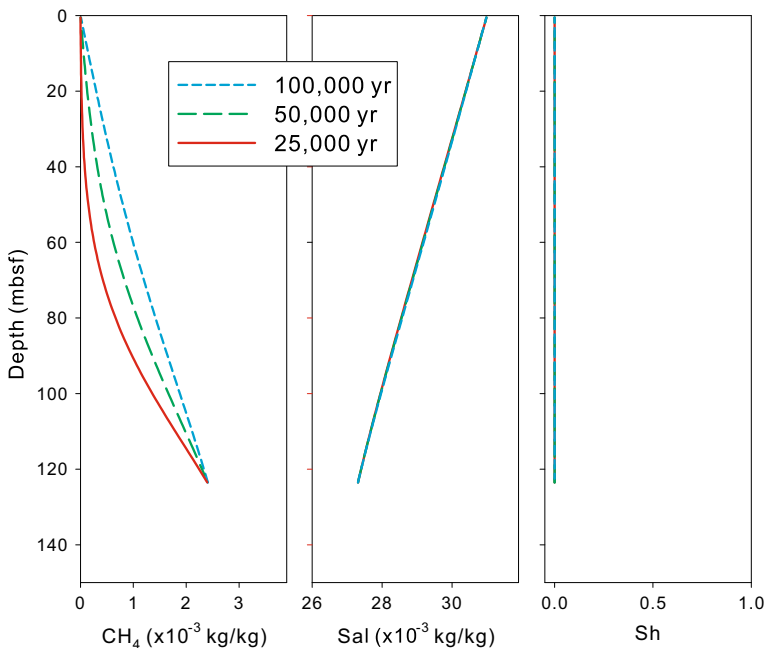


Fig. 6 Model results of Case 1 for the fluid system with a small Peclet number (4E-6). In this case, diffusion alone is not sufficient to deliver enough methane to form gas hydrate

gas hydrate saturation reaches more than 30% after 100 kyr of simulation. This is in contrast to Cases 1 and 2 with Peclet numbers smaller or equal to 1.

However, even with very strong advection in Case 3, no brine is formed at any depth in the sediments. On the contrary, due to the strong fluid advection prescribed in this scenario, the whole sediment column is flushed with the freshwater. Such result contradicts the observations from our study sites, where shallow brine coexists with the abundant gas hydrate in the sediments in the upper 100 mbsf as in Fig. 5. A similar case study applied in Torres et al. (2004) to Hydrate Ridge led the authors to conclude that the methane transport exclusively by advection is not sufficient to sustain the hydrate formation rate required to produce the

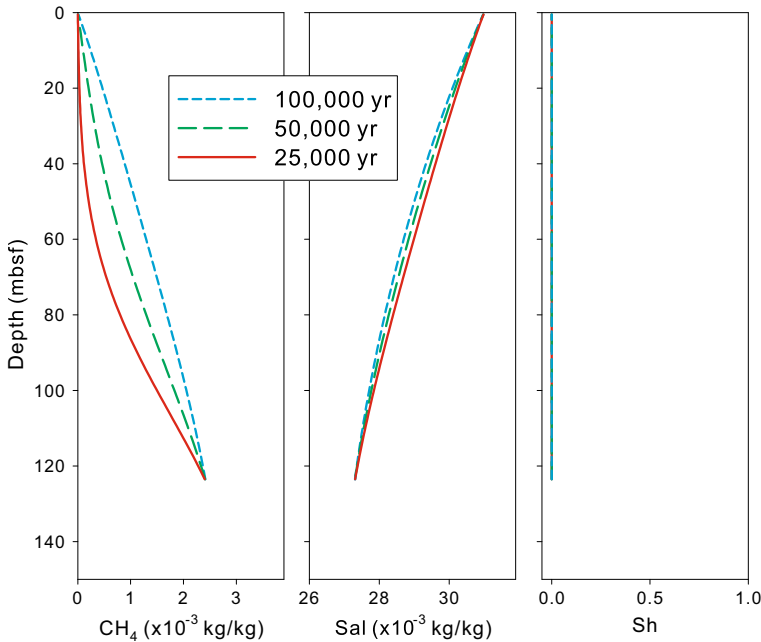


Fig. 7 Model results of Case 2 for the fluid system with Pecllet number close to 1. Even though the advection component is stronger in this case compared to Case 1, still not enough methane delivered for gas hydrate formation within the simulation time

observed salinity enrichment. A different source of methane other than aqueous transport from depth was postulated in Torres et al. (2004) to be required.

In Case 4, we postulate therefore the existence of a source of methane $f_M \neq 0$ in the sediment section where abundant gas hydrate was observed (17 mbsf at UBGH2-7). In this simulation, we use minimum advective flux (Peclet number $\ll 1$ as in Table 5) and show that in response to the strong methane input, gas hydrate saturation exceeds the highest saturation obtained in Case 3 within 5 kyr. Because of the rapid formation of methane hydrate, dissolved ions accumulate in the pore fluids faster than are lost by diffusion to the overlying bottom water, leading to a brine patch above 50 mbsf. After running the model for 10 kyr, the hydrate saturation exceeds 60% and the salinity is 1.5 times higher than χ_{1S}^{sw} in bottom seawater, a value that is similar to what we observed in the pore water profiles in Fig. 9.

In Case 5 shown in Fig. 10, we include both large advective flux q and an arbitrary methane source $f_M \neq 0$. Similarly as in Case 4, gas hydrate saturation increases rapidly around the depths where methane source is present. However, the salinity enrichment in Case 5 is different than that observed in Case 4: The highest value is smaller, and the profile is nonsymmetric because some of the salt is transported toward the seafloor by strong fluid advection.

We note that in Cases 4 and 5, one might argue that pressure Eq. (21) should be solved to account for the local value of $\nabla \cdot q = f = f_M$ instead of assuming $\nabla \cdot q = 0$. However, the methanogenesis represented by f_M turns carbon from solid phase (organic matter) to dissolved phase (dissolved methane in pore fluid) and does not introduce new carbon into the overall system, thus $f = 0$.

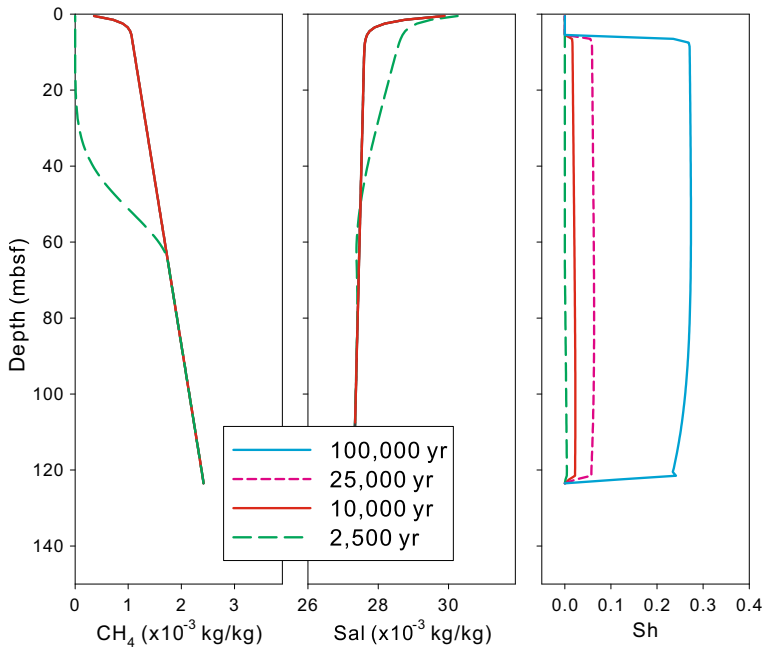


Fig. 8 Model results of Case 3 for the fluid system with larger Peclet number. Methane is rapidly delivered by advection to form the gas hydrate in the entire sediment column. Salinity, however, decreases due to the effective delivery of fresh fluid from the bottom. This salinity trend is different from the observations

5.2 Discussion

The model (2) appears to reproduce the two-way coupled dynamics, and the hydrate and salinity profiles, in a manner consistent with the intuition. Furthermore, Case 4 gives results which are close to the profiles recorded in experiments. However, the presence of large source of methane f_M is needed to create the shallow brine patches, and the magnitude of f_M is not fully explained.

5.2.1 Limitations of the Model in Its Ability to Explain the Experimental Data

As shown in Hong et al. (2014), microbial methane production through organic matter degradation initiates at the depth where sulfate in the pore water is depleted and methane concentration starts to increase, i.e., in sulfate–methane transition zone (SMTZ). The depth of microbial methane production may correspond to the location of the brine patches observed in Ulleung Basin. Therefore, in Case 4, we tested whether in situ methanogenesis could provide the methane required to sustain the rapid hydrate formation. Methanogenesis rates in Ulleung Basin, estimated from one chimney and one nonchimney site using a kinetic model constrained by pore water data, range from a few to ≈ 25 mmol/m³/year Hong et al. (2014). Using the unit conversion (22), we see that the rate f_M assumed in Case 4 is significantly higher than the realistic rate of methanogenesis estimated in Hong et al. (2014). In other words, the rate f_M proposed in Hong et al. (2014) is not large enough to account simultaneously for rapid gas hydrate formation and the associated shallow brine observed in Ulleung Basin.

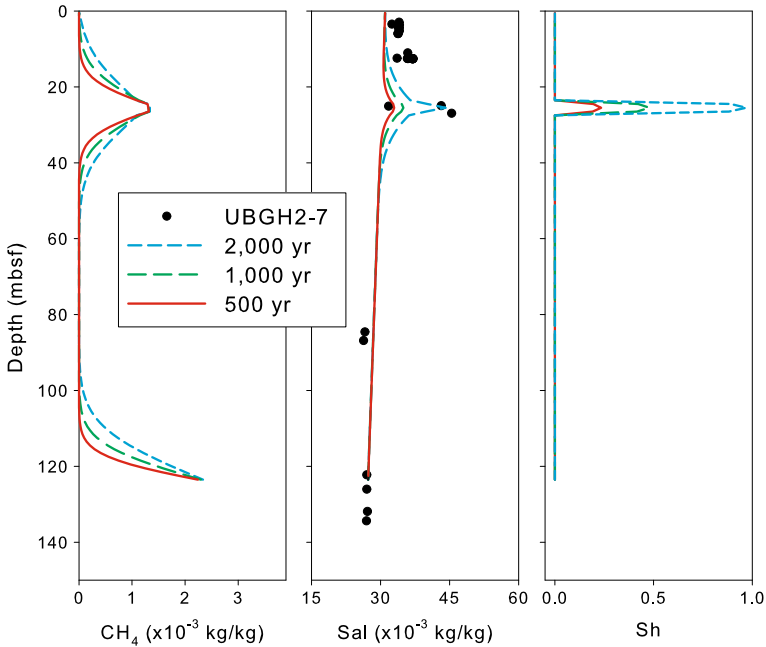


Fig. 9 Model results of Case 4 for the fluid system with a small Peclet number and a methane source term at 25 mbsf. The observed salinity enrichment is similar to that for experimental data by adding an arbitrary source of methane. The source term contributes large quantity of methane in a short time sufficient for rapid hydrate formation which in turn creates the salinity spike. Due to the insignificant advection component assigned in this case, diffusion is not strong enough to erase such salinity spike

As another possible explanation, one might argue that there might be a lateral advective transport of gas which might provide the source of methane. However, the seismic and chemistry analyses presented in [Kim et al. \(2013\)](#), [Hong et al. \(2014\)](#) suggest that most of the methane is generated below the SMTZ, or even deeper, and move upward as imaged in seismics, with no lateral advection.

Thus, while the simulation gives results consistent with the data, further hypotheses are needed to explain the observations.

5.2.2 Inclusion of Gas Phase

Similarly to the reasoning used in [Torres et al. \(2004\)](#) for the Hydrate Ridge case, we are led to conclude that the methane in the Ulleung Basin sites discussed here must be advecting in the gas phase from below the model domain. The methane solubility is too low for fluid advection to supply enough methane, with advection rate slow enough not to erase the positive salinity lense. Most likely, there is a source of gas below the HSZ, as imaged in seismic data, but free gas cannot travel through HSZ in the model (2) nor in the comprehensive models ([Liu and Flemings 2008](#)) since these assume that water is abundant. Liu and Flemings in [Liu and Flemings \(2006\)](#) hypothesized that the positive salinity anomaly that results from rapid hydrate formation at the base of the HSZ sustains a local three-phase equilibrium that allows methane gas to migrate upward and extends the saline tongue throughout the HSZ. Such extended positive salinity anomaly is, however, not observed in Ulleung Basin. Rather,

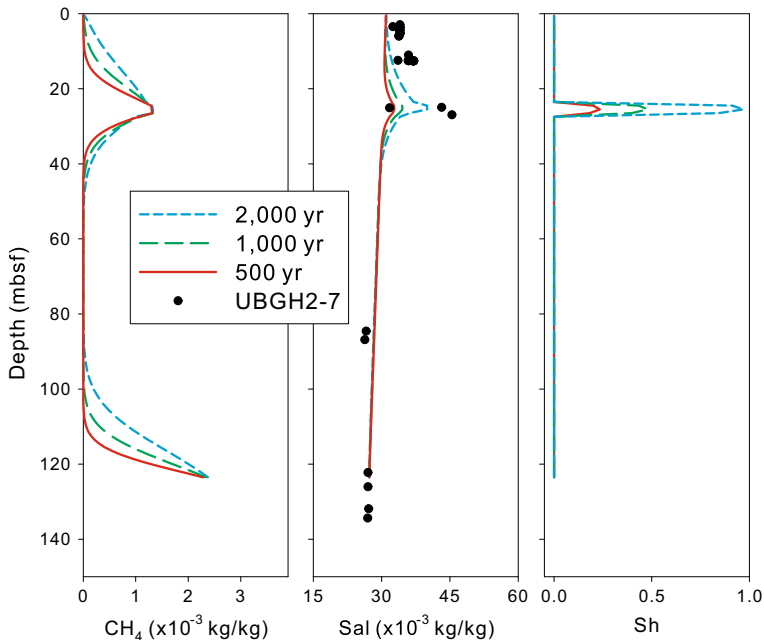


Fig. 10 Model results of Case 5 and the fluid system with a large Peclet number and a methane source term. Similar to the results from Case 4, large quantity of gas hydrate forms in less than 2000 years. The salinity enrichment is smaller compared to Case 4, and its profile is nonsymmetric due to the more effective fluid transport by larger advection

the observed profiles as in Fig. 5 show that the brine is confined to shallow depths less than 50 mbsf, and to salinities lower than seawater salinities at depths greater than that.

5.3 Salinity Dependence

Furthermore, according to the P_{eq} calculations for UBGH2-7 in the pressure range (21.65–22.90) and the temperature range (273.55–294.8), at the depth of the salinity spikes between 20–30 mbsf, we cannot have free gas phase, even if salinity equals double the seawater value. Therefore, our conclusions from simulation results are not affected by the particular approximations made to obtain the reduced phase equilibria model. In addition, the difference in salinity data that can be attributed to the measurements shipboard versus in situ does not change our conclusions.

Further extensions of the model, and in particular the inclusion of methane transport in the gas phase, are therefore needed to explain the particular salinity spikes and are outside the present scope.

6 Conclusions

In this paper, we presented a reduced model of transport of methane and salt dissolved in liquid phase, with accompanying methane hydrate formation. The model was obtained from the comprehensive model in Liu and Flemings (2008) after several simplifying assumptions were made. These assumptions are easily justified for basin modeling and make our reduced

model very compact, efficient, and easily amenable to the various analyses. The model is easily calibrated using phase behavior described in the literature, and we described in detail good agreement between various empirical and algebraic models. Thus, our paper provides a bridge between the practical and useful models and the rigorous mathematical model and computational analyses, and thus represents a useful tool for modeling the dynamic gas hydrate evolution in marine systems. In addition, it opens the door to various new computational simulations while it can be calibrated with the experimental data.

We were able to obtain good quantitative agreement between the model results and the data from Ulleung Basin by providing an additional methane source within the modeled domain, but note that in situ methanogenesis is not sufficient to generate the needed methane. In addition, the presence of fresh fluids at depth in Ulleung Basin sites that host near-seafloor brine patches argues against the development of a large positive salinity anomaly rising from the base of the HSZ to the seafloor, which could support methane transport through the HSZ as proposed by others, e.g., [Liu and Flemings \(2006\)](#). Our results are consistent with previous work by [Torres et al. \(2004\)](#) and [Torres et al. \(2011\)](#). However, we stress that since neither in situ methanogenesis nor transport within a salinity front are consistent with Ulleung Basin data, there must be a separate process supplying enough methane, so that the salinity spikes that accompany near-surface gas hydrate patches can be sustained.

Acknowledgments We would like to thank the anonymous referees whose remarks helped to improve the manuscript.

Open Access This article is distributed under the terms of the Creative Commons Attribution 4.0 International License (<http://creativecommons.org/licenses/by/4.0/>), which permits unrestricted use, distribution, and reproduction in any medium, provided you give appropriate credit to the original author(s) and the source, provide a link to the Creative Commons license, and indicate if changes were made.

Appendix

For completeness, we recall here the details on modeling as well as certain auxiliary conversion factors.

Derivation of Reduced Model

The conservation of mass for the methane component in hydrate zone ([Liu and Flemings 2008](#)) takes the form

$$\frac{\partial}{\partial t} (\phi_0 (S_l \rho_l \chi_{lM} + S_h \rho_h \chi_{hM})) + \nabla \cdot (q \rho_l \chi_{lM}) - \nabla \cdot (D_{lM} \rho_l \nabla \chi_{lM}) = \bar{f}_M. \quad (15)$$

In this equation, \bar{f}_M is an external source of methane, e.g., due to bacteria-induced methanogenesis.

The accumulation part (the term under the time derivative) can be rewritten with $N_M = \frac{\bar{N}_M}{\rho_l}$ as

$$N_M \rho_l = \bar{N}_M = S_l \rho_l \chi_{lM} + S_h \rho_h \chi_{hM} = S_l \chi_{lM} + (1 - S_l) R.$$

where the (dimensionless) quantity R is

$$R := \frac{\rho_h \chi_{hM}}{\rho_l} \approx \text{const}, \quad (16)$$

Note that \bar{N}_M is the total mass of methane per unit volume which accounts for the methane present both in the liquid and hydrate phases, and N_M is its dimensionless counterpart, relative to brine density.

Finally, it is useful to see that $S_I(x, t; N_M)$ is a function

$$S_I = \frac{N_M - R}{\chi_{IM} - R} = \begin{cases} 1, & N_M \leq \chi_{IM}^{\max}(x, t), \\ \frac{N_M - R}{\chi_{IM}^{\max}(x, t) - R}, & N_M > \chi_{IM}^{\max}(x), \end{cases} \tag{17}$$

Upon $f_M := \frac{\bar{f}_M}{\rho_l}$, and rescaling, we rewrite (15) in the form (2a).

Next, mass conservation for salt has the form

$$\frac{\partial}{\partial t} (\phi_0(S_I \rho_l \chi_{IS})) + \nabla \cdot (q \rho_l \chi_{IS}) - \nabla \cdot (D_{IS} \rho_l \nabla \chi_{IS}) = \bar{f}_S. \tag{18}$$

and that for water

$$\frac{\partial}{\partial t} (\phi_0(S_I \rho_l \chi_{IW} + S_h \rho_h \chi_{hW})) + \nabla \cdot (q \rho_l \chi_{IW}) - \nabla \cdot (D_{IW} \rho_l \nabla \chi_{IW}) = \bar{f}_W. \tag{19}$$

The structure of these equations is similar to that of (15) except that the salinity component is not present in the hydrate phase. Based on (1a), we can divide (18) by ρ_l ; renaming $\chi_{IS} = \chi_{IS}$, we obtain the salinity part of (2).

Pressure Equation

To derive the pressure equation, we add (15), (18), (19). Collecting terms and taking into account volume constraints $S_I + S_h = 1$ as well as $\chi_{IM} + \chi_{IS} + \chi_{IW} = 1$ and $\chi_{kM} + \chi_{hW} = 1$, we see that the accumulation term becomes $\frac{\partial}{\partial t} \phi_0(S_I \rho_l + S_h \rho_h)$. The advection term becomes $\nabla \cdot (q \rho_l)$, and the diffusion term

$$\begin{aligned} R_D &:= -\nabla \cdot (S_I \rho_l \phi_0 (D_M^0 \nabla \chi_{IM} + D_W^0 \nabla \chi_{IW} + D_S^0 \nabla \chi_{IS})) \\ &= -\nabla \cdot (S_I \rho_l \phi_0 (D_M^0 \nabla \chi_{IM} + D_W^0 \nabla (1 - \chi_{IM} - \chi_{IS}) + D_S^0 \nabla \chi_{IS})) \\ &= -\nabla \cdot (S_I \rho_l \phi_0 ((D_M^0 - D_W^0) \nabla \chi_{IM} + (D_S^0 - D_W^0) \nabla \chi_{IS})). \end{aligned} \tag{20}$$

Assuming that all diffusivities are equal, $\nabla \sum_{C=M,W,S} \chi_{IC} = \nabla(1) = 0$ and the diffusion term R_D vanishes. After further simplifications based on (1a), we obtain

$$\frac{\partial}{\partial t} \left(\phi_0 \left(S_I \left(1 - \frac{\rho_h}{\rho_l} \right) + \frac{\rho_h}{\rho_l} \right) \right) + \nabla \cdot q = f,$$

where $f = f_M + f_S + f_W$. If furthermore ϕ_0 is assumed constant in time, and $\rho_h \approx \rho_l$, then, after some algebra, we obtain the steady-state pressure equation

$$\nabla \cdot q = f. \tag{21a}$$

The Eq. (21a) is coupled with Darcy’s law

$$q = -\frac{K}{\mu} (\nabla P_1 - \rho_l G \nabla D(x)) \tag{21b}$$

In the absence of sources and $f \equiv 0$, q is divergence free. In the 1D case, $q = const$ and is equal to the flux across the boundary $\partial\Omega$. In fact, due to low fluxes q , the pressure is usually close to the hydrostatic $P_1^0(x)$ pressure defined by (1b).

Conversion Factors

The conversion factor between χ_{IS} and χ_{IS}^m is computed as follows. Assume we have 1L seawater with weight 1.03 kg=1030 g. Let the salinity be $\chi_{IS} = 0.035$ kg/kg. In the volume of 1L, this corresponds to $0.035 \times 1030 = 36.05$ g. Using molecular mass of 58.44g/mol of NaCl, we see that this gives $36.05/58.44 = 0.62$ moles of NaCl. The same volume 1L of seawater has $N = 1030/18.02 = 57.2$ moles, since 18.02 g/mol is the molecular weight of water. Thus, the mole fraction corresponding to $\chi_{IS} = 0.035$ kg/kg and $S = 35$ g/kg is therefore $\chi_{IS}^m = 0.62/(0.62 + 57.2) = 0.01$.

Further conversion factors are needed. In particular, for f_M , we have

$$\begin{aligned} & 1 \frac{\text{mmol}}{\text{m}^3 \text{year}} \\ &= 10^{-3} \frac{\text{mol}}{\text{m}^3 \text{year}} \times 16 \frac{\text{g}}{\text{mol}} \times 10^{-3} \frac{\text{kg}(\text{CH}_4)}{\text{g}} \times \frac{1}{1030} \frac{\text{m}^3}{\text{kg}(\text{SW})} \times 1000 \frac{\text{year}}{\text{kyr}} \\ &= 1.55 \times 10^{-5} \frac{\text{kg}(\text{CH}_4)}{\text{kg}(\text{SW}) \text{ kyr}} \end{aligned} \quad (22)$$

References

- Bahk, J., Kim, G.Y.: Characterization of gas hydrate reservoirs in the Ulleung Basin, East Sea (Korea), by integration of core and log data. *Mar. Pet. Geol.* **47**, 30–42 (2013)
- Ballard, A.L.: A non-ideal hydrate solid solution model for a multi-phase equilibria program. Technical report, Colorado School of Mines (2002)
- Barrer, R., Stuart, W.: Non-stoichiometric clathrate compounds of water. *Proc. R. Soc. Lond. Ser. A Math. Phys. Sci.* **243**(1233), 172–189 (1957)
- Bear, J., Cheng, A.: *Modeling Groundwater Flow and Contaminant Transport*. Springer, New York (2010)
- Center for Hydrate Research Software CSMHYD and CSMGem. <http://hydrates.mines.edu/CHR/Software.html>. Accessed 9 April 2015
- Class, H., Helmig, R., Bastian, P.: Numerical simulation of non-isothermal multiphase multicomponent processes in porous media 1. An efficient solution technique. *Adv. Water Res.* **25**, 533–550 (2002)
- Collett, T., Bahk, J.J., Baker, R., Boswell, R., Divins, D., Frye, M., Goldberg, D., Husebø, J., Koh, C., Malone, M., et al.: Methane hydrates in nature current knowledge and challenges. *J. Chem. Eng. Data* **60**(2), 319–329 (2014)
- Daigle, H., Dugan, B.: Capillary controls on methane hydrate distribution and fracturing in advective systems. *Geochem. Geophys. Geosyst.* **12**(1), Q01003 (2011). doi:10.1029/2010GC003392
- Davie, M., Zatsepina, O.Y., Buffett, B.: Methane solubility in marine hydrate environments. *Mar. Geol.* **203**(1), 177–184 (2004). doi:10.1016/s0025-3227(03)00331-1
- De Roo, J., Peters, C., Lichtenthaler, R., Diepen, G.: Occurrence of methane hydrate in saturated and unsaturated solutions of sodium chloride and water in dependence of temperature and pressure. *AIChE J.* **29**(4), 651–657 (1983)
- Dholabhai, P., Englezos, P., Kalogerakis, N., Bishnoi, P.: Equilibrium conditions for methane hydrate formation in aqueous mixed electrolyte solutions. *Can. J. Chem. Eng.* **69**(3), 800–805 (1991)
- Dickens, G.R.: Rethinking the global carbon cycle with a large, dynamic and microbially mediated gas hydrate capacitor. *Earth Planet. Sci. Lett.* **213**, 169–183 (2003)
- Dullien, F.: *Porous Media*. Academic Press, San Diego (1979)
- Garg, S., Pritchett, J., Katoh, A., Baba, K., Fijii, T.: A mathematical model for the formation and dissociation of methane hydrates in the marine environment. *J. Geophys. Res.* **113**, B08,201 (2008)
- Gibson, N.L., Medina, F.P., Peszynska, M., Showalter, R.E.: Evolution of phase transitions in methane hydrate. *J. Math. Anal. Appl.* **409**(2), 816–833 (2014). doi:10.1016/j.jmaa.2013.07.023
- Hong, W.L., Torres, M.E., Kim, J.H., Choi, J., Bahk, J.J.: Towards quantifying the reaction network around the sulfate-methane-transition-zone in the Ulleung Basin, East Sea, with a kinetic modeling approach. *Geochim. Cosmochim. Acta* **140**, 127–141 (2014). doi:10.1016/j.gca.2014.05.032

- Horozal, S., Lee, G.H., Bo, Y.Y., Yoo, D.G., Park, K.P., Lee, H.Y., Kim, W., Kim, H.J., Lee, K.: Seismic indicators of gas hydrate and associated gas in the ulleung basin, east sea (japan sea) and implications of heat flows derived from depths of the bottom-simulating reflector. *Mar. Geol.* **258**(1), 126–138 (2009)
- Kim, J.H., Torres, M.E., Hong, W.L., Choi, J., Riedel, M., Bahk, J.J., Kim, S.H.: Pore fluid chemistry from the Second Gas Hydrate Drilling Expedition in the Ulleung Basin (UBGH2): Source, mechanisms and consequences of fluid freshening in the central part of the Ulleung Basin, East Sea. *Mar. Pet. Geol.* **47**, 99–112 (2013). doi:[10.1016/j.marpetgeo.2012.12.011](https://doi.org/10.1016/j.marpetgeo.2012.12.011)
- Kim, Y., Lim, B., Lee, J., Lee, C.: Solubilities of carbon dioxide, methane, and ethane in sodium chloride solution containing gas hydrate. *J. Chem. Eng. Data* **53**(6), 1351–1354 (2008)
- Kim, Y., Ryu, S., Yang, S., Lee, C.: Liquid water-hydrate equilibrium measurements and unified predictions of hydrate-containing phase equilibria for methane, ethane, propane, and their mixtures. *Ind. Eng. Chem. Res.* **42**, 2409–2414 (2003)
- Kobayashi, R., Withrow, H., Williams, G., Katz, D.: Gas hydrate formation with brine and ethanol solutions. In: *Proceeding of the 30th Annual Convention, Natural Gasoline Association of America*, pp. 27–31 (1951)
- Lake, L.W.: *Enhanced Oil Recovery*. Prentice Hall, New Jersey (1989)
- Lee, J., Kim, G.Y., Kang, N., Yi, B.Y., Jung, J., Im, J.H., Son, B.K., Bahk, J.J., Chun, J.H., Ryu, B.J., et al.: Physical properties of sediments from the ulleung basin, east sea: results from second ulleung basin gas hydrate drilling expedition, east sea (Korea). *Mar. Pet. Geol.* **47**, 43–55 (2013)
- Liu, X., Flemings, P.B.: Passing gas through the hydrate stability zone at southern hydrate ridge, offshore oregon. *Earth Planet. Sci. Lett.* **241**(1), 211–226 (2006)
- Liu, X., Flemings, P.B.: Dynamic multiphase flow model of hydrate formation in marine sediments. *J. Geophys. Res.* **112**, B03,101 (2008)
- Lu, Q., Peszynska, M., Wheeler, M.F.: A parallel multi-block black-oil model in multi-model implementation. *SPE J.* **7**(3), 278–287 (2002). SPE 79535
- Lu, W., Chou, I., Burruss, R.: Determination of methane concentrations in water in equilibrium with si methane hydrate in the absence of a vapor phase by in situ raman spectroscopy. *Geochim. Cosmochim. Acta* **72**, 412–422 (2008)
- Maekawa, T., Itoh, S., Sakata, S., Igari, S.I., Imai, N.: Pressure and temperature conditions for methane hydrate dissociation in sodium chloride solutions. *Geochem. J.* **29**, 325–330 (1995)
- Malinverno, A., Kastner, M., Torres, M., Wortmann, U.: Gas hydrate occurrence from pore water chlorinity and downhole logs in a transect across the northern cascadia margin (integrated ocean drilling program expedition 311). *J. Geophys. Res.* **113**, B08,103 (2008)
- Milkov, A.V., Dickens, G.R., Claypool, G.E., Lee, Y.J., Borowski, W.S., Torres, M.E., Xu, W., Tomaru, H., Tréhu, A.M., Schultheiss, P.: Co-existence of gas hydrate, free gas, and brine within the regional gas hydrate stability zone at hydrate ridge (oregon margin): evidence from prolonged degassing of a pressurized core. *Earth Planet. Sci. Lett.* **222**(3–4), 829–843 (2004). doi:[10.1016/j.epsl.2004.03.028](https://doi.org/10.1016/j.epsl.2004.03.028)
- Nimblett, J., Ruppel, C.: Permeability evolution during the formation of gas hydrates in marine sediments. *J. Geophys. Res.* **108**, B9, 2420 (2003)
- Peszynska, M., Lu, Q., Wheeler, M.F.: Multiphysics coupling of codes. In: Bentley, L.R., Sykes, J.F., Brebbia, C.A., Gray, W.G., Pinder, G.F. (eds.) *Computational Methods in Water Resources*, pp. 175–182. A. A. Balkema, Boca Raton (2000)
- Peszynska, M., Medina, F.P., Hong, W.-L., Torres, M.E.: Reduced numerical model for methane hydrate formation under conditions of variable salinity. Time-stepping variants and sensitivity. *Computation* **4**(1), 1 (2016). doi:[10.3390/computation4010001](https://doi.org/10.3390/computation4010001)
- Peszynska, M., Showalter, R.E., Webster, J.T.: Advection of methane in the hydrate zone: model, analysis and examples. *Math. Methods Appl. Sci.* **38**(18), 4613–4629 (2015)
- Peszynska, M., Torres, M., Tréhu, A.: Adaptive modeling of methane hydrates. In: *International Conference on Computational Science, ICCS 2010, Procedia Computer Science*, vol. 1, pp. 709–717. www.elsevier.com/locate/procedia and www.sciencedirect.com (2010)
- Pitzer, K.S.: *Activity Coefficients in Electrolyte Solutions*. CRC Press, Boca Raton (1991)
- Platteeuw, J., der Waals, J.V.: Thermodynamic properties of gas hydrates II: Phase equilibria in the system H₂S–C₃H₈–H₂O at -3 C. *Recueil des Travaux Chimiques des Pays-Bas* **78**, 126–133 (1959)
- Rempel, A.W.: Hydromechanical processes in freezing soils. *Vadose Zone J.* (2012). doi:[10.2136/vzj2012.0045](https://doi.org/10.2136/vzj2012.0045)
- Riedel, M., Collett, T., Kim, H.S., Bahk, J.J., Kim, J.H., Ryu, B.J., Kim, G.: Large-scale depositional characteristics of the ulleung basin and its impact on electrical resistivity and archie-parameters for gas hydrate saturation estimates. *Mar. Pet. Geol.* **47**, 222–235 (2013)
- Scientists, U.: *Ulleung basin gas hydrate drilling expedition 2. Preliminary report. Technical report, KIGAM* (2010)

- Sloan, E., Koh, C.A.: *Clathrate Hydrates of Natural Gases*, 3rd edn. CRC Press, Boca Raton (2008)
- Tishchenko, P., Hensen, C., Wallmann, K., Wong, C.S.: Calculation of stability and solubility of methane hydrate in seawater. *Chem. Geol.* **219**, 37–52 (2005). doi:[10.1016/j.chemgeo.2005.02.008](https://doi.org/10.1016/j.chemgeo.2005.02.008)
- Torres, M., Wallmann, K., Tréhu, A., Bohrmann, G., Borowski, W., Tomaru, H.: Gas hydrate growth, methane transport, and chloride enrichment at the southern summit of Hydrate Ridge, Cascadia margin off Oregon. *Earth Planet. Sci. Lett.* **226**(1–2), 225–241 (2004). doi:[10.1016/j.epsl.2004.07.029](https://doi.org/10.1016/j.epsl.2004.07.029)
- Torres, M.E., Kim, J.H., Choi, J., Ryu, B.J., Bahk, J.J., Riedel, M., Collett, T.S., Hong, W., Kastner, M.: Occurrence of high salinity fluids associated with massive near-seafloor gas hydrate deposits. In: *Proceedings of the 7th International Conference on Gas Hydrates (ICGH 2011)*, Edinburgh, Scotland, United Kingdom (2011)
- Trehu, A.M., Flemings, P., Bangs, N.L., Chevalier, J., Gracia, E., Johnson, J.E., Liu, C.S., Liu, X., Riedel, M., Torres, M.: Feeding methane vents and gas hydrate deposits at south hydrate ridge. *Geophys. Res. Lett.* **31**(L23), 310 (2004)
- Xu, W., Ruppel, C.: Predicting the occurrence, distribution, and evolution of methane hydrate in porous marine sediments. *J. Geophys. Res.* **104**, 5081–5095 (1999)
- Zatsepina, O., Buffett, B.: Phase equilibrium of gas hydrate: implications for the formation of hydrate in the deep sea floor. *Geophys. Res. Lett.* **24**(13), 1567–1570 (1997). doi:[10.1029/97GL01599](https://doi.org/10.1029/97GL01599)
- Zatsepina, O., Buffett, B.: Thermodynamic conditions for the stability of gas hydrate in the seafloor. *J. Geophys. Res. Solid Earth* **103**(B10), 24127–24139 (1998). doi:[10.1029/98jb02137](https://doi.org/10.1029/98jb02137)

Widespread methane seepage along the continental margin off Svalbard - from Bjørnøya to Kongsfjorden

S. Mau*¹, M. Römer¹, M. E. Torres², I. Bussmann³, T. Pape¹, E. Damm³, P. Geprägs¹, P. Wintersteller¹, C.-W. Hsu¹, M. Loher¹, G. Bohrmann¹, and shipboard scientific party HE449 and HE450

¹ MARUM – Center for Marine Environmental Sciences and Department of Geosciences, University of Bremen, Klagenfurter Str., 28359 Bremen, Germany

² College of Oceanic and Atmospheric Sciences, Oregon State University, 104 Ocean Admin Building, Corvallis, Oregon 97331-5503

³ Alfred Wegener Institute Helmholtz Centre for Polar and Marine Research, Am Handelshafen 27570 Bremerhaven, Germany

* Corresponding author: Susan Mau, e-mail: smau@marum.de

Numerous articles have recently reported on gas seepage offshore Svalbard, because of gas emission that may be due to gas hydrate dissociation, possibly triggered by anthropogenic ocean warming. Here we report on findings for a much broader extent of seepage in water depths at and shallower than the gas hydrate stability zone. More than a thousand gas seepage sites imaged as acoustic flares generate a 600 kilometer-long plume. Most flares were detected in the vicinity of the Hornsund Fracture Zone. We postulate that the gas ascends from depth along the fracture zone; its discharge is focused on bathymetric highs and is constrained by glaciomarine and Holocene sediments in the troughs. A fraction of this dissolved methane (~1.8%) was oxidized whereas a minor but measureable fraction (0.05%) was transferred into the atmosphere in August 2015. The large scale seepage reported here is not linked to anthropogenic warming.

Fluid geochemistry from a shallow water gas hydrate pingo field south of Svalbard: the role of gas hydrate in fluid transport

(abstract submitted to Gas in Marine Sediments Conference, Tromsø, Norway, September 2016)

Wei-Li Hong, Marta E. Torres, Brian Haley, and Evan A. Solomon

We present porewater geochemistry data from 7 gravity cores in a newly discovered gas hydrate field of the Storfjordrenna area (water depth ~380m), 50km south of Svalbard. The concentration of major (Ca, Mg, K, Sr) and minor (Li, B, Ba) elements; $\delta^{18}\text{O}$, δD of pore fluid and the and $^{87}\text{Sr}/^{86}\text{Sr}$ in dissolved phase are indicative of fluid sources and water-rock interactions. Concentrations of dissolved inorganic carbon (DIC), total alkalinity, hydrogen sulfide as well as $\delta^{13}\text{C}$ of the DIC were measured to investigate biogeochemical reactions.

Our observations confirm the significance of various biogeochemical reactions on fluid geochemistry. High concentrations of hydrogen sulfide, DIC, and alkalinity indicate rapid turnover of methane and sulfate through anaerobic oxidation of methane (AOM). This reaction fuels precipitation of authigenic carbonates, which largely determines the concentrations of Mg and Ca at sites with strong methane supply. Methane at these sites is transported in the gas phase and leads to the formation of gas hydrate in the upper 80 cmbsf. Gas hydrate formation may block fluid transport from depth. Oxygen (1 ‰) and hydrogen (2.5 ‰) isotopes of pore water are enriched relative to SMOW, but the data suggest influence of glacial melt water, rather than a gas hydrate signal.

The fluid systems beneath different pingos are contrastingly different. We detected enrichments of Li (up to 64 μM) and Sr (up to 96 μM) in one of the pingo sites, while these elements are depleted (13 μM in Li and 70 μM in Sr) at another pingo that is only ~1km away. Boron concentrations are generally lower than the bottom seawater concentration in all the cores investigated (250 to 300 μM). The enriched strontium isotopic ratios (up to 0.70987) measured at various sites suggest influence of weathering of continental material, a reaction that also explains the enrichment of Li and Sr in a few sites.

In general, the fluid at sites where the methane supply is weak, and show no evidence of gas hydrate formation, are enriched in ^{87}Sr , indicating influence of silicate weathering and deep fluid migration. On the other hand, in sites with strong methane flux and abundant gas hydrate, the strontium isotopic ratios are close to seawater indicating very little deep fluid contribution. We hypothesize that the transport of methane is decoupled from the transport of fluid. Gas hydrate seems to prevent upward migration of fluid and may lead to accumulation of methane gas beneath the hydrate.

National Energy Technology Laboratory

626 Cochrans Mill Road
P.O. Box 10940
Pittsburgh, PA 15236-0940

3610 Collins Ferry Road
P.O. Box 880
Morgantown, WV 26507-0880

13131 Dairy Ashford, Suite 225
Sugarland, TX 77478

1450 Queen Avenue SW
Albany, OR 97321-2198

2175 University Ave. South
Suite 201
Fairbanks, AK 99709

Visit the NETL website at:
www.netl.doe.gov

Customer Service:
1-800-553-7681

